© 2021. Published by The Company of Biologists Ltd | Journal of Cell Science (2021) 134, jcs252916. doi:10.1242/jcs.252916

RESEARCH ARTICLE

Coupling of dynamic microtubules to F-actin by Fmn2 regulates chemotaxis of neuronal growth cones

Tanushree Kundu[1,‡], Priyanka Dutta[1,*,‡], Dhriti Nagar[1], Sankar Maiti[2] and Aurnab Ghose[1,§]

ABSTRACT

Dynamic co-regulation of the actin and microtubule subsystems enables the highly precise and adaptive remodelling of the cytoskeleton necessary for critical cellular processes, such as axonal pathfinding. The modes and mediators of this interpolymer crosstalk, however, are inadequately understood. We identify Fmn2, a non-diaphanous-related formin associated with cognitive disabilities, as a novel regulator of cooperative actin–microtubule remodelling in growth cones of both chick and zebrafish neurons. We show that Fmn2 stabilizes microtubules in the growth cones of cultured spinal neurons and *in vivo*. Super-resolution imaging revealed that Fmn2 facilitates guidance of exploratory microtubules along actin bundles into the chemosensory filopodia. Using live imaging, biochemistry and single-molecule assays, we show that a C-terminal domain in Fmn2 is necessary for the dynamic association between microtubules and actin filaments. In the absence of the cross-bridging function of Fmn2, filopodial capture of microtubules is compromised, resulting in destabilized filopodial protrusions and deficits in growth cone chemotaxis. Our results uncover a critical function for Fmn2 in actin–microtubule crosstalk in neurons and demonstrate that the modulation of microtubule dynamics via associations with F-actin is central to directional motility.

KEY WORDS: Actin–microtubule crosstalk, Formin-2, Fmn2, Axon guidance, Growth cone, Filopodia

INTRODUCTION

The actin and microtubule subsystems of the cellular cytoskeleton are essential for the organization of the cytoplasm, cell and tissue morphogenesis, and cellular motility. It is increasingly apparent that crosstalk between these two cytoskeleton systems is essential for regulating core cellular processes and that their dynamic remodelling is functionally coordinated (Coles and Bradke, 2015; Dogterom and Koenderink, 2019). Growth cone-mediated axonal extension and pathfinding necessitates dynamic coordination between the peripheral filamentous actin (F-actin) and the exploratory microtubules (MTs) and is necessary for the establishment of neural circuits (Coles and Bradke, 2015; Dogterom and Koenderink, 2019; Lowery and Van Vactor, 2009; Vitriol and Zheng, 2012).

[1]Indian Institute of Science Education and Research (IISER) Pune, Dr Homi Bhabha Road, Pune 411008, India. [2]Department of Biological Sciences, Indian Institute of Science Education and Research Kolkata, Mohanpur 741246, Nadia, West Bengal, India.
*Present address: National Centre for Cell Science, NCCS Complex, S.P. Pune University Campus, Ganeshkhind, Pune 411007, India.
‡These authors contributed equally to this work

§Author for correspondence (aurnab@iiserpune.ac.in)

P.D., 0000-0002-8490-5813; A.G., 0000-0002-2053-3918

Handling Editor: Michael Way
Received 11 August 2020; Accepted 26 May 2021

The central (C)-domain of the growth cone is enriched with stable MTs extending from the axon shaft. While most of the stable MTs are confined to the C-domain, few dynamic MTs explore the peripheral (P)-domain and interact with F-actin structures in the leading edge lamellipodia and filopodia. Filopodia are chemosensory structures composed of parallel F-actin filaments and are essential for chemotactic guidance. Stabilization of filopodia in the direction of growth cone turning mediates directional motility of growth cones. Guidance cue signalling biases the activity of exploratory MTs to the direction of turning, increasing their entry and stabilization within filopodia on that side (Buck and Zheng, 2002; Mack et al., 2000; Sabry et al., 1991; Williamson et al., 1996). Biased MT stabilization in filopodia, by ensuring long-lived tracks for cargo transport and increasing mechanical resilience, supports filopodial stability and promotes growth cone turning. The entry and capture of MTs in filopodia involves dynamic associations between the exploratory MT and the F-actin structures in the transition (T)- and P-domains of the growth cones. The F-actin bundles of filopodia appear to serve as tracks for extending MTs (Schaefer et al., 2002; Zhou et al., 2002) and may facilitate growth cone extension. The activities mediating the critical association of MTs with F-actin in neuronal growth cones are only beginning to be identified (Biswas and Kalil, 2018; Liu et al., 2010; Slater et al., 2019; Szikora et al., 2017).

Formin-2 (Fmn2) is a non-diaphanous-related formin whose expression is enriched in developing and mature mammalian nervous systems (Leader and Leder, 2000; Sahasrabudhe et al., 2016). Biallelic loss of Fmn2 and heterozygous deletions in Fmn2 have been associated with human intellectual disability (Almuqbil et al., 2013; Law et al., 2014). Mutations in Fmn2 have been found in a subpopulation of children with sensory processing dysfunction (Marco et al., 2018). Fmn2 expression has been found to be reduced in post-mortem brain samples of patients with post-traumatic stress disorder and Alzheimer's disease (Agis-Balboa et al., 2017). In rodents, loss of Fmn2 has been associated with accelerated age-associated memory impairment and amyloid-induced deregulation of gene expression (Agis-Balboa et al., 2017; Peleg et al., 2010); however, little is known about the mechanisms underpinning Fmn2 function in the brain. We have previously shown that Fmn2 regulates axonal outgrowth and pathfinding in chick spinal commissural neurons *in vivo* (Sahasrabudhe et al., 2016). This study identified Fmn2 function in stabilizing the adhesive contacts of the growth cone with the extracellular matrix (ECM). Furthermore, reduced Fmn2 in spinal commissural neurons leads to aberrant axonal trajectories *in vivo*, suggestive of chemotactic deficits (Sahasrabudhe et al., 2016).

As deficits in chemotactic responses could result from aberrant MT dynamics, we explored Fmn2 function in the regulation of MT dynamics in growth cones. We discovered that Fmn2 facilitates the exploration of MTs into the P-domain of the growth cones by guiding MTs into filopodia by physically coupling them to F-actin

Journal of Cell Science (2021) 134, jcs252916. doi:10.1242/jcs.252916

bundles. This cross-linking is necessary to stabilize MTs. *In vitro* reconstitution assays confirmed F-actin–MT cross-bridging by Fmn2 via its C-terminal FSI domain. Fmn2-mediated MT capture in filopodia appears to be critical for filopodial dynamics and stability and regulates growth cone turning. This work identifies Fmn2 as novel mediator of synchronized co-organization of the F-actin and MT cytoskeletons in neuronal growth cones, underscoring Fmn2 function in neural development.

RESULTS

Fmn2 regulates microtubule organization in neuronal growth cones

Previously we have identified Fmn2 as a regulator of growth cone motility and guidance, both *in vitro* and *in vivo* (Sahasrabudhe et al., 2016). Fmn2 is localized to F-actin rich structures, such as F-actin bundles in growth cone filopodia and stress fibres in fibroblasts (Sahasrabudhe et al., 2016). As MTs are involved in growth cone steering and are themselves subject to guidance along actin bundles (Schaefer et al., 2002), we investigated the role of Fmn2 in regulating MT dynamics in the growth cone.

Immunolocalization of Fmn2 in growth cones of chick spinal commissural neurons showed enrichment of Fmn2 along the length of filopodial F-actin bundles extending all the way to the base of these bundles (Fig. 1A–A‴; also shown previously by Sahasrabudhe et al., 2016). To test Fmn2 function in MT organization, we depleted Fmn2 using specific translation-blocking morpholinos (Fmn2-MO; see Materials and Methods for characterization) that resulted in at least 75% reduction in endogenous Fmn2 levels (Fig. S1A) followed by evaluation of MTs (anti-α-tubulin immunofluorescence) and F-actin (phalloidin immunofluorescence) using stimulated emission depletion (STED) nanoscopy (Fig. 1B,C). As reported previously (Sahasrabudhe et al., 2016), depletion of Fmn2 reduced the number and length of growth cone filopodia compared to those of non-specific control morpholino (Ctl-MO)-treated neurons (Fig. 1D,E) along with a reduction in growth cone area (Fig. S1B). Interestingly, Fmn2-MO treatment resulted in a reduced proportion of filopodia with detectable MTs (Fig. 1F; 41.47±5.13% in Ctl-MO-treated neurons compared with 23.88±6.01% following Fmn2 knockdown; mean±s.e.m.). Furthermore, though the number of MT ends in the growth cones (Fig. 1G) and the growth cone area occupied by MTs (Fig. S1C) were comparable between Ctl-MO- and Fmn2-MO-transfected neurons, the fraction of MTs invading filopodia was reduced by almost 50% upon Fmn2 depletion (Fig. 1H; 28.77±3.90% in control treatments compared with 13.66±3.69% in Fmn2-MO-transfected growth cones).

Association and co-alignment with F-actin bundles have been proposed to guide MTs from the central region of the growth cone into the peripheral filopodia (Sabry et al., 1991; Schaefer et al., 2002; Zhou et al., 2002). We, therefore, evaluated the co-alignment of MTs with actin bundles in the peripheral zone (lamellipodial region and filopodia) of the growth cones. Fmn2 was found to promote alignment of MTs with F-actin bundles. The proportion of MTs aligned with actin bundles was drastically reduced from 71.61±4.44% in control neurons to 34.88±4.27% upon knockdown of Fmn2 (Fig. 1I). Furthermore, the distance over which the two polymers co-aligned also decreased upon reduction of Fmn2 expression (Fig. 1J).

These results implicate Fmn2 as a novel regulator of MT organization in growth cones. Our observations suggest that Fmn2 mediates the association between MTs and F-actin bundles, thereby facilitating MT exploration of the peripheral zone and entry into filopodia.

Microtubule dynamics and stability in growth cones is regulated by Fmn2

To examine Fmn2-dependent regulation of MTs in growth cones, we evaluated MT dynamics by imaging EGFP-tagged MT plus-end-tracking protein (+TIP), EB3 (also known as MAPRE3). The plusTipTracker algorithm (Applegate et al., 2011; Matov et al., 2010) was used to quantify EB3 dynamics (Fig. 2A–B′; Movies 1, 2). Although the average number of dynamic MT tips in growth cones was comparable (Fig. S2A), the mean growth speed of MTs in the Fmn2-MO-treated growth cones (8.49 ±0.59 µm/min; mean±s.e.m.) was higher compared with that in controls (6.29±0.45 µm/min; Fig. 2C). Consistent with this observation, the growth length of the polymerizing MTs also increased from 0.87±0.07 µm in Ctl-MO-transfected neurons to 1.17±0.33 µm in Fmn2-MO-treated growth cones (Fig. 2D). However, the MT growth lifetimes remained unchanged (Fig. 2E; 7.67±0.59 s in control and 7.83±0.39 s in Fmn2-knockdown cells). Fmn2 knockdown resulted in an increase in the overall MT dynamicity (collective growth speeds of all comet tracks over their collective lifetimes; 7.45±0.44 µm/min and 5.67±0.39 µm/min in Fmn2-MO-treated cells and Ctl-MO-treated cells, respectively; Fig. 2F).

Because the analysis of EB3 dynamics upon Fmn2 knockdown suggested an overall decrease in the stability of the MT cytoskeleton, we tested whether this observation was consistent with changes in the levels of detyrosinated tubulin – a tubulin posttranslational modification associated with long-lived, stable MTs. A mask of the area occupied by total tubulin immunofluorescence was used to limit the boundaries of the MT network, and the fluorescence intensity of detyrosinated tubulin within this mask was quantified. Indeed, Fmn2 depletion reduced the detyrosinated α-tubulin:total MT ratio in growth cones (Fig. 2G–I).

Collectively, these data suggest that Fmn2 is an important regulator of MT dynamics in growth cones and promotes the stability of the MT network.

Fmn2 regulates microtubule dynamics in growth cones *in vivo*

To evaluate the role of Fmn2 in growth cone MT dynamics *in vivo*, we expressed fluorescently tagged EB3 in the Rohon–Beard (RB) neurons of larval zebrafish. Growth cones of the peripheral axons of the RB neurons expressing the reporter protein were evaluated in zebrafish embryos at 22 hours post fertilization (hpf) (Fig. 2J; Movies 3, 4). A splice-blocking morpholino against zebrafish Fmn2b (Zf-Fmn2-MO; see Materials and Methods for characterization; Fig. S2B) was used to deplete functional Fmn2. Compared to non-specific morpholino (Ctl-MO)-injected animals, injection of Zf-Fmn2-MO resulted in increased growth speeds (5.782±0.2419 µm/min in Ctl-MO neurons compared to 6.764±0.2774 µm/min in Zf-Fmn2-MO neurons; mean±s.e.m.; Fig. 2K) and shorter growth lifetimes (47.75±3.035 s in Ctl-MO neurons compared to 34.49±1.908 s in Zf-Fmn2-MO neurons; Fig. 2L) of EB3 comets in RB neuron growth cones. These data indicate that depletion of Fmn2 *in vivo* alters MT dynamics in growth cones and is suggestive of an MT regulatory function that is conserved across phyla and neuronal subtypes.

Microtubule stability in filopodia requires Fmn2

Exploratory MTs are guided into filopodia by co-alignment with F-actin bundles (Schaefer et al., 2002; Slater et al., 2019). As both the proportion of filopodia invaded by MTs and the number of MTs entering filopodia were reduced upon Fmn2 knockdown

Journal of Cell Science (2021) 134, jcs252916. doi:10.1242/jcs.252916

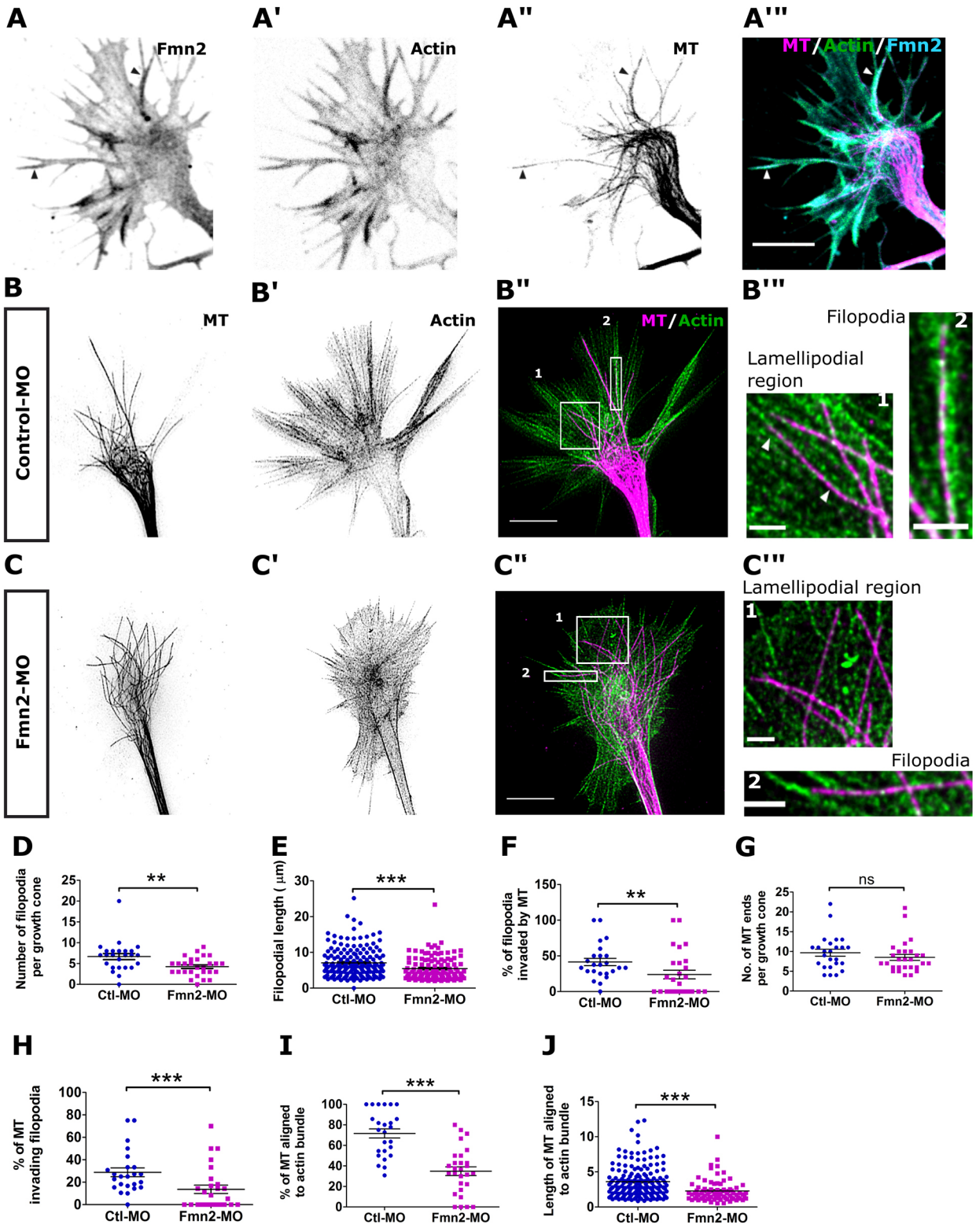

Fig. 1. See next page for legend.

(Fig. 1F,H), we evaluated the EB3 dynamics specifically within filopodia of the growth cones of chick spinal neurons.

Growing dynamic MTs showed a characteristic reduction in velocity as they entered filopodia from the central region of the growth cone, presumably due to retardation of growth speed resulting from direct interactions with filopodial actin bundles (Fig. 3A). However, in growth cones depleted of Fmn2, no change in the velocity was observed as MTs polymerized from the central region to enter filopodia (Fig. 3B). This observation suggests that Fmn2 may mediate the association of the invading MT with the filopodial F-actin bundle. Given the localization of Fmn2 along the entire length of the filopodial actin bundle, it is ideally positioned to

Journal of Cell Science (2021) 134, jcs252916. doi:10.1242/jcs.252916

Fig. 1. Fmn2 colocalizes with F-actin and MTs in filopodia and promotes actin–MT alignment in the peripheral regions of the growth cone. (A–A‴) Representative micrographs of triple immunostaining using specific antibodies showing endogenous localization of Fmn2 (greyscale in A and cyan in A‴), actin (greyscale in A′ and green in A‴) and MTs (greyscale in A″ and magenta in A‴), as well as an overlayed image of all three (A‴). Fmn2 decorates the entire filopodia, and Fmn2–actin-enriched filopodia are frequently occupied by MTs, as shown by arrowheads. Scale bar: 5 µm. The data shown is representative of two independent experiments. (B–C‴) Representative STED micrographs of actin and MTs in (B–B‴) Ctl-MO- and (C–C‴) Fmn2-MO-treated growth cones. The alignment of MTs (greyscale in B and C; magenta in merge panels) with actin (greyscale in B′ and C′; green in merge panels) occurs in regions peripheral from the centre of the growth cone. Numbered boxes in B″ and C″ indicate regions shown in B‴ and C‴, respectively. (B‴) Magnified images showing alignment of MTs and actin in lamellipodial region and filopodia in a Ctl-MO-treated growth cone. Arrowheads indicate co-alignment of MTs with F-actin. (C‴) Magnified images showing lack of such alignment in an Fmn2-MO-treated growth cone. Scale bars: 5 µm (B″,C″), 1 µm (B‴,C‴). (D) Quantification of filopodia number per growth cone (Ctl-MO, n=25; Fmn2-MO, n=28; P=0.0035) and (E) growth cone filopodial lengths (Ctl-MO, n=168; Fmn2-MO, n=118; P=0.0002). (F) Percentage of filopodia per growth cone invaded by MTs in Ctl-MO (n=24) compared to Fmn2-MO (n=27) (P=0.0078). (G) Quantification of MT ends per growth cone in Ctl-MO- (n=25) and Fmn2-MO-treated cells (n=28) shows that numbers are comparable (P=0.1943) even though (H) the proportion of MT invading filopodia per growth cone is reduced in Fmn2-MO-treated cells compared to control (Ctl-MO, n=24; Fmn2-MO, n=27; P=0.0008). (I) The percentage of MTs aligned to actin per growth cone in the peripheral zone (lamellipodial and filopodial regions) (Ctl-MO, n=24; Fmn2-MO, n=27; P<0.0001) and (J) the lengths over which the actin and MTs are co-aligned (Ctl-MO, n=161; Fmn2-MO, n=78; P<0.0001) are much higher in Ctl-MO-treated growth cones than in Fmn2-depleted growth cones. In D–J, the mean±s.e.m. is indicated, and data shown are from more than three independent experiments. ***P<0.001; **P<0.01; ns, P>0.05 (Mann–Whitney test).

guide exploratory MTs into filopodia. Consistent with these observations, in Fmn2-knockdown neurons the growth speed of MTs inside filopodia was found to be higher (9.72±0.52 µm/min; mean±s.e.m.) compared to that in control neurons (7.31±0.29 µm/min; Fig. 3C); however, the lifetime of the EB3 comets within filopodia was reduced by 50% upon Fmn2 depletion (Fig. 3D; 86.40±7.58 s in Ctl-MO-treated filopodia and 40.91±5.35 s in Fmn2-MO-treated filopodia). The incursion distance of EB3 comets inside filopodia was unaltered between control and Fmn2-MO-treated neurons (Fig. S3).

The reduction in the dwell time of EB3 comets in filopodia is suggestive of loss of MT stability. We probed this further by measuring MT catastrophe events directly using fluorescently tagged α-tubulin. This analysis revealed that MT catastrophe was more frequent upon Fmn2 knockdown as the latency for the first catastrophe event following incursion into a filopodia was much shorter (Fig. 3E; 4.00±0.61 s for Fmn2-MO and 9.30±1.42 s for Ctl-MO; mean±s.e.m.). The propensity for catastrophe possibly accounts for the short-lived dwell times of EB3 comets in filopodia. Furthermore, the velocity of retraction or shrinkage during catastrophe of MTs within filopodia in Fmn2-MO-transfected neurons (14.13±2.08 µm/min) was significantly higher than that in the Ctl-MO-treated filopodia (9.87±0.76 µm/min) (Fig. 3F). The latter observation is consistent with an Fmn2-dependent association between MT and filopodial F-actin that prevents rapid retraction of a collapsing MT filament.

Filopodial F-actin bundles undergo retrograde flow, and the invading MT, owing to its association with these actin bundles, also experiences this retrograde movement (Schaefer et al., 2002). This behaviour can be captured in kymographs of EB3 comets inside filopodia as sporadic rearward movement (retrograde events) and apparent cessation of forward progress (stall) despite ongoing MT polymerization, as evident by the persistence of the EB3 signal at the tip of the invading MT (Fig. 3G,H) (Liu et al., 2010). As expected, the reduction of F-actin retrograde flow upon treatment with the myosin-II inhibitor blebbistatin made the EB3 trajectories smoother and decreased the EB3 retrograde events and stalls (Fig. 3I; 1.23±0.24 events with DMSO treatment compared to 0.49±0.13 events with blebbistatin treatment; mean±s.e.m.). EB3–mCherry was used to visualize MT dynamics in the experiments involving blebbistatin to prevent inactivation of the drug by blue light. More significantly, knockdown of Fmn2 resulted in a reduction of retrograde and stall events and much smoother MT growth trajectories inside filopodia (Fig. 3J; 2.14±0.30 events in Ctl-MO-treated growth cones compared to 0.9±0.23 events in Fmn2-MO-treated growth cones) suggesting the involvement of Fmn2 in mediating the association between MTs and filopodial F-actin.

Taken together, these data indicate that Fmn2 not only mediates the capture and guidance of exploratory MTs into filopodia, but also regulates the stability of the invasive MT within the filopodia. Thus, Fmn2, directly or indirectly, cross-links the polymerizing MTs to the filopodial F-actin bundles.

Fmn2 directly binds and bundles F-actin and microtubules

In vitro studies of the *Drosophila* formin, Cappuccino (Capu), indicate that the Capu C-terminal FSI domain mediates charge-based interaction with both F-actin and MTs (Roth-Johnson et al., 2014). Alignment of Capu and chick Fmn2 FSI domains revealed a high degree of homology, including the conservation of the basic amino acid residues mediating the charge-based interactions of Capu with F-actin and MTs (Fig. S4A). To directly probe the interactions of Fmn2 with actin and MTs, we purified recombinant proteins corresponding to the FH2FSI and FH2-ΔFSI regions of the chick Fmn2 protein (Fig. 4A,B). The actin-binding activities of these proteins were tested using a conventional high-speed co-sedimentation assay. FH2FSI and FH2-ΔFSI bound to actin filaments with apparent equilibrium constants (K_D) of 5.0±0.2 µM and 12.5±0.1 µM, respectively (mean±s.e.m.; Fig. 4C; Fig. S4B,C). These findings demonstrate that FH2FSI has a higher affinity for F-actin than FH2-ΔFSI.

We further investigated the MT-binding ability of FH2FSI and FH2-ΔFSI in a high-speed co-sedimentation assay. Our data revealed that Fmn2 FH2FSI has significantly higher affinity for Taxol-stabilized MTs than FH2-ΔFSI, with K_D of 1.6±0.1 µM and 18.6±0.1 µM, respectively (Fig. 4D; Fig. S4D,E). While the co-sedimentation studies reported here (Fig. 4) were conducted using standard protocols (F-actin, 50 mM salt; MT, 0 mM salt), we also undertook similar analyses using salt concentrations ranging from 0 mM to 150 mM (Fig. S5). These studies revealed the continued association of Fmn2 with both F-actin or MTs for all the salt concentrations tested (Fig. S5). Thus, Fmn2 is capable of binding both F-actin and MTs directly, and the FSI domain is a key component of these associations.

Apart from binding F-actin, FH2FSI was also capable of bundling F-actin filaments, as demonstrated by low-speed co-sedimentation assays and total internal reflection fluorescence (TIRF) microscopy of labelled F-actin filaments (Fig. 4E,G; Fig. S4F). In contrast, FH2-ΔFSI was incapable of bundling actin filaments (Fig. 4E,G; Fig. S4G). Low speed co-sedimentation with Taxol-stabilized MTs revealed that FH2FSI, but not FH2-ΔFSI, could also bundle MTs in a concentration-dependent manner (Fig. 4F; Fig. S4H,I). This observation was confirmed using TIRF imaging of labelled MTs in the presence of recombinant proteins

Journal of Cell Science (2021) 134, jcs252916. doi:10.1242/jcs.252916

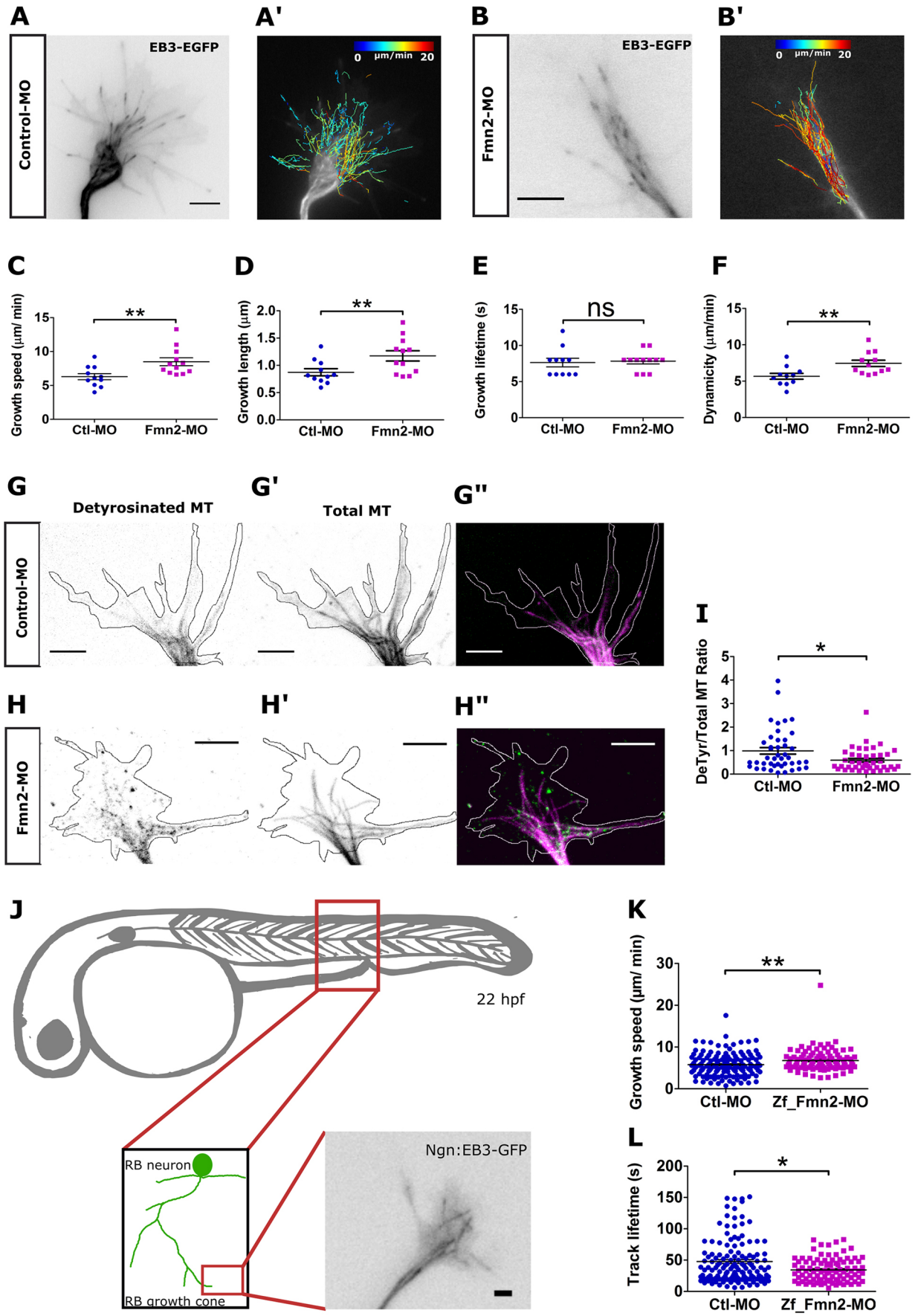

Fig. 2. See next page for legend.

Journal of Cell Science (2021) 134, jcs252916. doi:10.1242/jcs.252916

Fig. 2. Knockdown of Fmn2 increases dynamicity and reduces stability of MTs in the growth cone. (A–B′) Representative growth cones labelled with the +TIP marker EB3–GFP in (A) Ctl-MO- and (B) Fmn2-MO-transfected growth cones. Time-lapse movies of EB3 were acquired at 2 s frame interval for 100 frames to measure MT polymerization. The analysis was performed using plusTipTracker software, and the comet tracks with overlaid colour-coded growth speeds are shown for Ctl-MO (A′) and for Fmn2-MO (B′). Scale bars: 5 µm. (C–F) Quantification of (C) mean MT growth speed (P=0.0089), (D) MT growth length (P=0.0210), (E) mean MT growth lifetime (P=0.5475) and (F) overall dynamicity of MT polymerization (P=0.0042) in Ctl-MO- (n=11; number of tracks=2917) and Fmn2-MO- (n=12; number of tracks=2426) transfected growth cones. In C–F, the mean±s.e.m. is indicated, and the data shown are from three independent experiments. **P<0.01; ns, P>0.05 (Mann–Whitney test). (G–H″) Representative images of detyrosinated (DeTyr) tubulin and total tubulin stained using specific antibodies in cells treated with Ctl-MO (G and G′, respectively) or Fmn2-MO (H and H′, respectively). Merge images (G″,H″) show DeTyr (green) and total MTs (magenta) with growth cones outlined by white lines. (I) The intensity of detyrosinated tubulin was measured within the area occupied by the total tubulin signal and normalized to total tubulin intensity (n=43 for Ctl-MO and n=42 for Fmn2-MO; P=0.0303). The mean±s.e.m. is indicated, and the data shown are from three independent experiments. *P<0.05 (Mann–Whitney test). Scale bars: 5 µm. (J) Schematic representation of a zebrafish larva at 22 hpf injected with *ngn1*: EB3–GFP. EB3–GFP is expressed in the Rohon–Beard (RB) neurons (inset). The second inset shows a representative image of the peripheral growth cone of an RB neuron displaying EB3 comets *in vivo*. Scale bar: 2 µm. (K) EB3 comet growth speeds increase (P=0.0033) while (L) the track lifetimes decrease (P=0.0200) upon knockdown of zebrafish Fmn2 using specific morpholinos (Zf-Fmn2-MO). EB3 comets were analysed using kymographs (Ctl-MO, n=134 comet tracks from from 13 growth cones; Fmn2-MO, n=95 tracks from 12 growth cones). The mean±s.e.m. is indicated, and the data shown are from two independent experiments. **P<0.01; *P<0.05 (Mann–Whitney test).

(Fig. 4G). Furthermore, we tested the ability of Fmn2 to protect MTs from cold shock-induced depolymerization. FH2FSI robustly stabilized MTs, indicating a role for Fmn2 in protecting MTs from depolymerization (Fig. S4J). To ensure that the fragments of Fmn2 used in these studies retained functionality we used *in vitro* actin nucleation assays to show that the FH2FSI fragment robustly nucleated F-actin (Fig. S6). The FH2-ΔFSI fragment was also capable of nucleating actin, albeit weakly (Fig. S6). These *in vitro* studies suggest that Fmn2 is a direct interactor of both F-actin and MTs, and the FSI domain is a major contributor to these interactions. Moreover, the FSI domain was found to be necessary for efficient bundling F-actin and MT filaments.

F-actin and microtubule filaments are cross-linked by Fmn2

The ability of Fmn2 to bind both F-actin and MTs led us to directly test the ability of Fmn2 to cross-link these two filament types. We visualized fluorescently labelled pre-polymerized phalloidin-stabilized F-actin and Taxol-stabilized MT filaments with and without FH2FSI or FH2-ΔFSI. In controls lacking Fmn2 fragments, randomly oriented single filaments of F-actin and MT were observed (Fig. 5A); however, in the presence of FH2FSI, F-actin and MT filaments co-aligned to form thick hybrid bundles (Fig. 5A). Conversely, the deletion of the FSI domain (FH2-ΔFSI) resulted in lack of co-alignment, and the filaments were randomly distributed as seen in the no protein control (Fig. 5A).

The F-actin–MT cross-linking ability of Fmn2 was further assessed using sedimentation assays. FH2FSI or FH2-ΔFSI were incubated with pre-polymerized phalloidin-stabilized F-actin and/or Taxol-stabilized MTs and centrifuged at very low speeds (2000 ***g***). The centrifugation conditions were optimized such that incubation of FH2FSI with MTs or F-actin alone resulted in partitioning of only a small amount of the polymers in the pellet fraction. However, incubation of FH2FSI with F-actin and MTs simultaneously resulted in a much larger amount of both the cytoskeleton polymers partitioning into the pellet fraction (Fig. 5B,D,E). These data indicate that Fmn2 interacts with both F-actin and MT filaments simultaneously and results in the formation of a larger hybrid complex. Incubation with FH2-ΔFSI failed to show similar cross-linking between MTs and F-actin (Fig. 5C–E).

To directly and dynamically visualize the formation of hybrid complexes and co-alignment between F-actin and MTs, we monitored the co-polymerization of the two cytoskeletal polymers using TIRF microscopy. MT and actin filaments were allowed to self-polymerize and elongate using tubulin dimers and actin monomers (a fraction of the tubulin dimers and actin monomers were fluorescently labelled; see Materials and Methods). In controls lacking Fmn2 protein, both F-actin and MT filaments were found to elongate but rarely contacted or associated with each other (Movie 5, Fig. S7). Strikingly, the presence of FH2FSI induced progressive co-alignment of the extending F-actin and MT filaments (Fig. 5F–H; Movie 6, Fig. S7). The association of the relatively more flexible F-actin filaments with the stiffer MTs resulted in progressive straightening of the F-actin filaments. In contrast, FH2-ΔFSI failed to co-align the two filaments. Thus, the FSI domain is critical for the simultaneous binding of Fmn2 dimers to both F-actin and MT filaments to promote cross-linking (Fig. 5F–H; Movie 7, Fig. S7).

Actin–microtubule cross-linking by Fmn2 is necessary for microtubule stability in filopodia

Because our *in vitro* studies demonstrated the requirement of the FSI domain in actin-MT cross-linking by Fmn2, we used the presence or absence of this domain in rescue experiments to directly probe Fmn2 function in growth cone filopodia. The cDNA for the mouse orthologue of Fmn2 (referred to here as mFmn2) lacks the binding sequence for anti-chick Fmn2 morpholinos and is thus resistant to knockdown using this reagent. EB3 dynamics within filopodia were evaluated following co-transfection with Fmn2-MO or Ctl-MO and morpholino-resistant mFmn2 constructs. Expression of the full-length mouse Fmn2 cDNA (mFmn2_FL) in the background of endogenous chick Fmn2 knockdown was able to rescue the defects observed in EB3 comet speed (Fig. 6A), dwell time (Fig. 6B) and the EB3 retrograde and/or stall events (Fig. 6C) inside filopodia. However, mouse Fmn2 lacking the FSI domain (mFmn2-ΔFSI) failed to rescue all these parameters (Fig. 6A–C). These rescue experiments demonstrate that, in agreement with our *in vitro* studies, Fmn2 regulates MT dynamics in filopodia by cross-linking MTs to the filopodial F-actin via the FSI domain.

Microtubule entry stabilizes filopodia

MT entry and capture within filopodia is known to stabilize filopodia and allow their extension (Barzik et al., 2014; Hu et al., 2012; McNeely et al., 2017). We tested the association between the presence of MTs within growth cone filopodia and filopodial lengths and lifetimes. We probed the association between the presence of MTs within filopodia and filopodial dynamics. Comparison of filopodial populations with and without MTs revealed a strong association between the presence of MTs and filopodial stability. In Ctl-MO-treated growth cones, immunofluorescence analysis using labelled phalloidin and antibodies against α-tubulin revealed that filopodia with detectable MTs were longer (9.64±0.59 µm; mean ±s.e.m.) than those lacking MTs (5.30±0.29 µm; Fig. 7A). Live-imaging studies tracking EB3 in filopodia further demonstrated that filopodia associated with MTs had longer lifetimes (100.0±16.33 s) than those without MTs (41.67±9.85 s; Fig. 7B). Importantly, the same trend was seen in Fmn2-depleted neurons. The filopodia not

Journal of Cell Science (2021) 134, jcs252916. doi:10.1242/jcs.252916

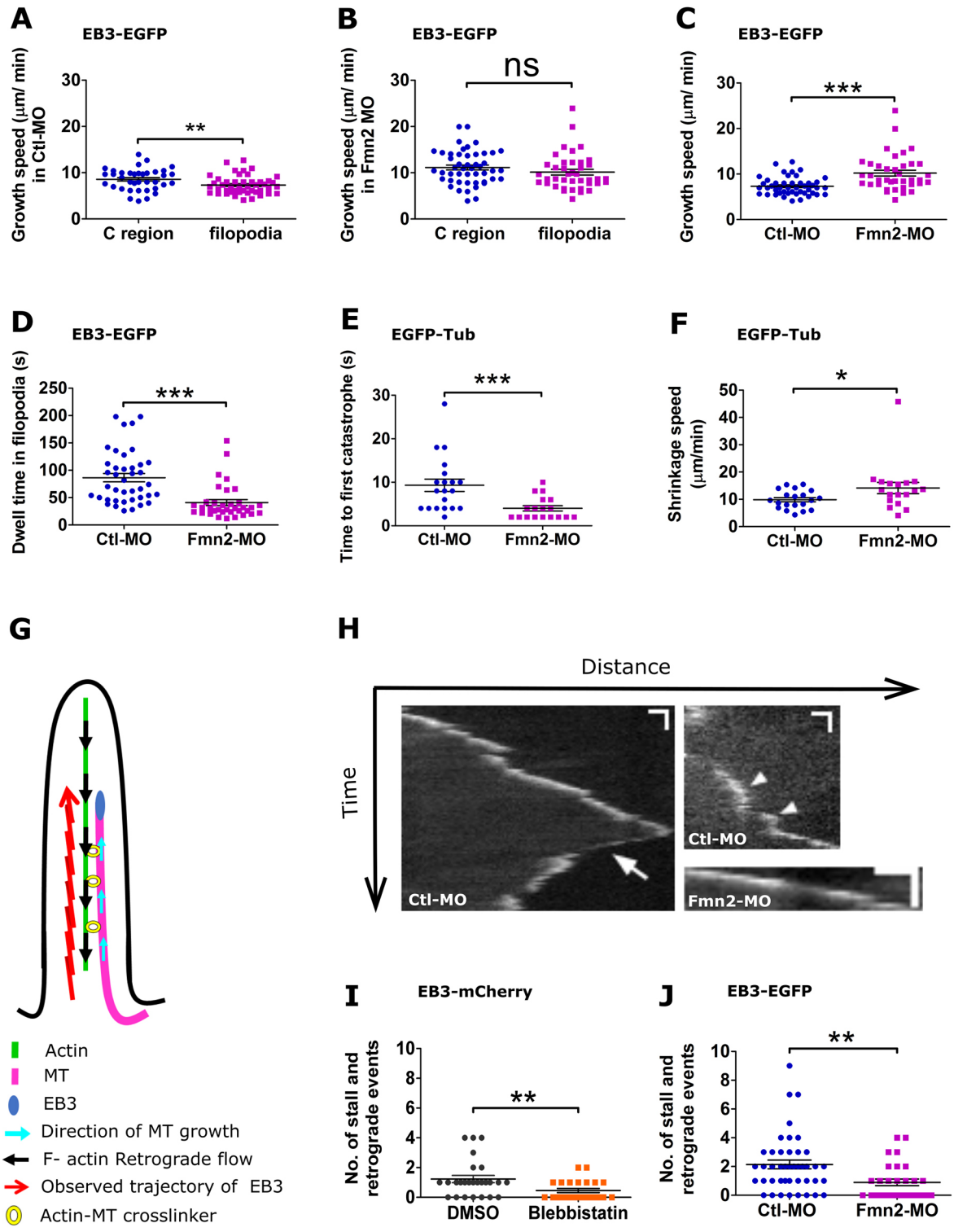

Fig. 3. See next page for legend.

containing MTs were shorter (4.81±0.28 µm) and also shorter-lived (48.22±7.71 s) compared to filopodia with MTs (7.84±0.81 µm and 67.60±10.04 s) (Fig. 7A,B). These results suggest that the reduced stability of MTs in filopodia (Fig. 3D–F) and the consequent reduction in the number of filopodia having MTs at any given time (Fig. 1F) are major contributors to the reduced filopodial lengths and lifetimes observed in Fmn2-depleted growth cones (Sahasrabudhe et al., 2016).

Fmn2 is required for growth cone turning at substrate borders

The deficits in MT entry into filopodia and the consequent reduction in filopodia stability are likely to influence the chemotactic response of Fmn2-depleted growth cones (Williamson et al., 1996; Zheng et al., 1996). We tested this proposition using a haptotactic border turning assay (Jean et al., 2012; Liu et al., 2010; Turney and Bridgman, 2005). Neurons were cultured on alternating stripes of

Journal of Cell Science (2021) 134, jcs252916. doi:10.1242/jcs.252916

Fig. 3. Fmn2 promotes MT stability in growth cone filopodia. (A,B) Growth speeds of EB3–GFP comets in the central region (C region) and filopodial region of growth cones treated with (A) Ctl-MO (C region, *n*=37; filopodia, *n*=46; *P*=0.0079) or (B) Fmn2-MO (C region, *n*=37; filopodia, *n*=38; *P*=0.0571). (C,D) Comparison of (C) growth speeds (Ctl-MO, *n*=46; Fmn2-MO, *n*=38; *P*<0.0001) and (D) dwell time (Ctl-MO, *n*=40; Fmn2-MO, *n*=35; *P*<0.0001) of EB3–GFP comets inside filopodia of Ctl-MO- and Fmn2-MO-treated growth cones. (E,F) Quantification of (E) time to first catastrophe after entering filopodia (Ctl-MO, *n*=20; Fmn2-MO, *n*=18; *P*=0.0008) and (F) catastrophe speed (Ctl-MO, *n*=20; Fmn2-MO, *n*=18; *P*=0.0209), measured using EGFP–tubulin in Ctl-MO- and Fmn2-MO-treated filopodia. (G) Schematic showing MT growth and observed trajectory of EB3 comets along actin bundles inside filopodia. The trajectories of EB3 comets appear jagged with retrograde and stall events. This is due to the coupling of the growing MT filament with F-actin, which itself is experiencing centripetally directed retrograde flow. (H) Representative kymographs of EB3–GFP showing retrograde (arrow) and stall (arrowhead) events in Ctl-MO- and Fmn2-MO-treated filopodia. Fmn2 knockdown decouples the growing MT from the filopodial F-actin and results in smoother trajectories, as seen in the Fmn2-MO kymograph. Scale bars: 10 µm, 10 s. (I) Quantification of retrograde and stall events using EB3–mCherry in the presence of blebbistatin treatment to reduce F-actin retrograde flow or of control DMSO treatment (*n*=26, DMSO; *n*=24, blebbistatin; *P*=0.0099). (J) Reduction in stall and retrograde events in EB3–GFP trajectories upon depletion of Fmn2 (Ctl-MO, *n*=43; Fmn2-MO, *n*=30; *P*=0.0014). In A–F,I,J, the mean±s.e.m. is indicated, and the data shown are from more than three independent experiments. ***P<0.001; **P<0.01; *P<0.05; ns, P>0.05 (Mann–Whitney test).

fibronectin plus laminin and poly-L-lysine (PLL) generated by microcontact printing, and were evaluated for growth cone turning behaviour at substrate borders (Fig. 7C,D). Although both surfaces were independently permissive for neuronal growth, growth cones of neurons plated on laminin plus fibronectin preferred to turn and continue to reside on the same substrate upon encountering the border with PLL. In Ctl-MO-transfected neurons, ∼73% of growth cones turned upon encountering the border (Fig. 7E,F); however, upon depletion of Fmn2, only ∼32% turned, whereas the majority crossed the border to grow into PLL (Fig. 7E,F). These observations indicate that aberrant chemotactic behaviour of Fmn2-knockdown growth cones, possibly originating from deficits in MT stabilization in filopodia, results in the inability to execute reliable growth cone turning at substrate borders.

DISCUSSION

Coordination and co-regulation of the actin and MT cytoskeletons are essential for key cellular processes, including motility and pathfinding of neuronal growth cones; however, our understanding of molecular activities mediating this crosstalk is limited. We identify the formin, Fmn2, as a novel mediator of actin–MT coordination in neuronal growth cones. Using a combination of *in vitro* biochemistry and cell biological analysis of spinal growth cones, we show that Fmn2 can directly interact with and cross-bridge F-actin and MTs, and this function is critical for growth cone dynamics and haptotaxis.

In non-neuronal cells, few members of the formin family have been implicated in actin–MT crosstalk. Formins are a family of 15 proteins (in mammals), most of which are also expressed in the nervous system (Dutta and Maiti, 2015; Krainer et al., 2013). These multi-domain proteins are commonly defined as actin nucleators, but they are emerging as cytoskeleton regulators with a diversity of functions and spatiotemporal regulation. Recent work has identified the ability of some formins to regulate MT dynamics. The +TIP protein, CLIP-170 (also known as CLIP1) has been shown to associate with the formin mDia1 (also known as DIAPH1) and accelerate F-actin polymerization at MT plus ends (Henty-Ridilla et al., 2016). Other members of the diaphanous-related formins (DRFs) have been found to influence MT stability in non-neuronal cells. Much less is known about formin-mediated actin–MT crosstalk in neurons. mDia1 activity has been associated with amyloid β-induced increase in MT stabilization in rodent neurons (Qu et al., 2017). In *Drosophila* neurons, the DRF formin DAAM has been shown to cross-link F-actin and MTs (Szikora et al., 2017). The expression of several formins in mammalian neurons suggests rich functional diversity of this family in the nervous system, conferring functional precision and adaptability on the neuronal cytoskeleton.

In recent years, several lines of evidence have accumulated that implicate Fmn2 function in neurodevelopment and neurodegeneration (Agis-Balboa et al., 2017; Almuqbil et al., 2013; Law et al., 2014; Marco et al., 2018); however, little is known about the mechanistic underpinnings of Fmn2 function in the nervous system. We have previously shown that Fmn2-depleted spinal commissural axons fail to cross the floor plate and show aberrant trajectories post crossing (Sahasrabudhe et al., 2016). Axonal pathfinding defects and deficits in the dynamics of chemosensory filopodia described in this previous study prompted us to evaluate Fmn2 function in coordinating MT–actin dynamics in the growth cone. Furthermore, in mouse oocytes, Fmn2 has been reported to bind MTs and associate with the spindle during metaphase I (Kwon et al., 2011).

We found that Fmn2 was necessary to stabilize MT dynamics in the growth cone. Depletion of Fmn2 resulted in increased MT dynamicity and polymerization accompanied by a reduction in the population of stable, long-lived detyrosinated MTs. STED nanoscopy revealed that co-alignment of F-actin bundles and MTs was reduced in Fmn2-knockdown growth cones. This observation implicates Fmn2 in regulating interpolymer associations between actin and MTs. Thus, the loss of association with F-actin may result in the observed changes in MT dynamics in the growth cone. Additionally, the ability of Fmn2 to bundle MT filaments and protect MTs from cold-shock-induced depolymerization are also likely to directly influence MT dynamics.

In the growth cone, MT movement occurs through both polymerization and motor-dependent MT sliding (Guha et al., 2021; Liu et al., 2010); however, the exploratory MTs that venture out from the C-domain into the peripheral filopodia are highly dynamic and grow via plus-end polymerization (Dillman et al., 1996; Guha et al., 2021; Schaefer et al., 2008). Because F-actin bundles are known to guide MTs into filopodia via direct or indirect interactions (Schaefer et al., 2002; Zhou et al., 2002), we conducted a detailed analysis of MT dynamics inside filopodia. Our data reveal two phenomena. First, Fmn2 along filopodial actin bundles mediates dynamic associations with exploratory MTs and guides them into filopodia (Fig. 7). Similar capture and redirection of MTs by F-actin bundles has previously been demonstrated *in vitro* (Preciado López et al., 2014). Second, in Fmn2-knockdown cells, despite a faster growth rate within the filopodia (possibly reflecting reduced dynamic interactions with F-actin), the invading MTs are unstable. Both the reduced dwell time of EB3 comets and increased predisposition to catastrophe, as seen in the GFP–tubulin studies, indicate reduction in stability. Ideally, marking the MT network with a fiduciary marker would have increased the precision of our analysis of EB3 dynamics; however, as the rates of MT polymerization (Szikora et al., 2017; Fig. 2C) are significantly higher than velocity of the bulk translocation of the entire MT network (Miller and Sheetz, 2006) we expect the contribution of the bulk movement to be negligible.

Journal of Cell Science (2021) 134, jcs252916. doi:10.1242/jcs.252916

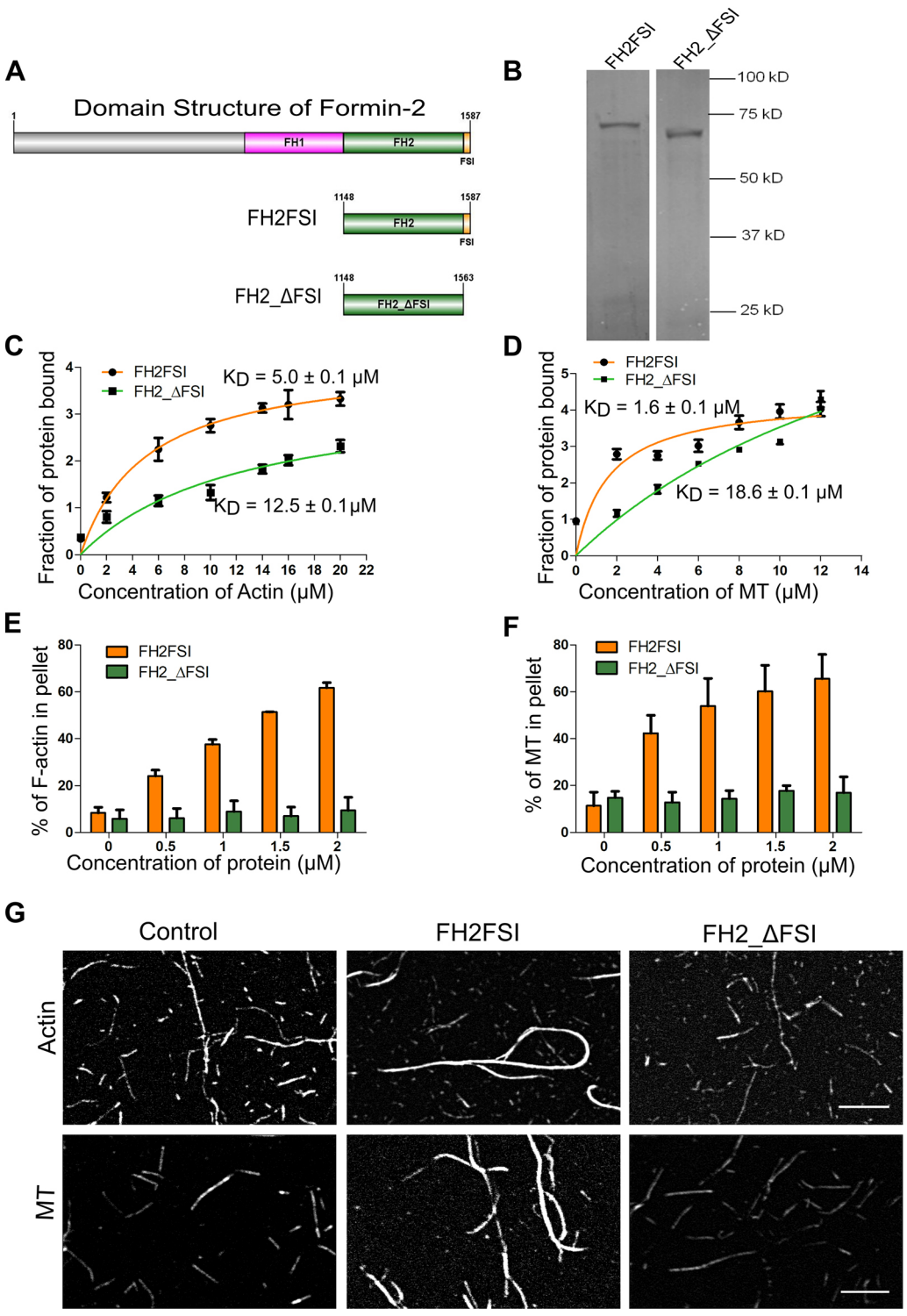

Fig. 4. Fmn2 can interact with and bundle both actin and MTs. (A) Schematic representation of the domain structure of chick Fmn2 and the different constructs used in this study. Numbers indicate amino acid residue positions. (B) Representative gel showing the expression of purified FH2FSI and FH2-ΔFSI fragments used for the study (kD, kilodaltons). (C) Binding of FH2FSI and FH2-ΔFSI to F-actin. Increasing concentrations of F-actin were incubated with each protein fragment (2 µM). The percentage of bound proteins was plotted against F-actin concentrations and fitted with a hyperbolic function. The K_D values for FH2FSI and FH2-ΔFSI are 5.0±0.1 µM and 12.5±0.1 µM, respectively (mean±s.d. from three independent experiments). (D) FH2FSI and FH2-ΔFSI binding affinity for MTs. Different concentrations of MTs were incubated with each protein fragment (2 µM). The amount of protein bound to MTs was fitted to a hyperbolic function for three independent reactions. The K_D values for FH2FSI and FH2-ΔFSI are 1.6±0.1 µM and 18.6±0.1 µM, respectively (mean±s.d. from four independent experiments). (E) Quantification of actin bundles in the presence of FH2FSI and FH2-ΔFSI from low-speed sedimentation assays for F-actin bundling. The data represents the mean±s.d. from three independent experiments. (F) Quantification of MT bundling by FH2FSI and FH2-ΔFSI from low-speed sedimentation assays for MT bundling. The data represents the mean±s.d. from three independent experiments. (G) Representative TIRF microscopy images of the F-actin (upper panels) and MT (lower panels) bundling reactions after incubation of 1 µM FH2FSI or 1 µM FH2-ΔFSI with sparsely labelled F-actin or MTs for 15 mins. Actin was labelled with Alexa Fluor 488–phalloidin and MTs were labelled using rhodamine-labelled tubulin. Scale bars: 5 µm.

Journal of Cell Science (2021) 134, jcs252916. doi:10.1242/jcs.252916

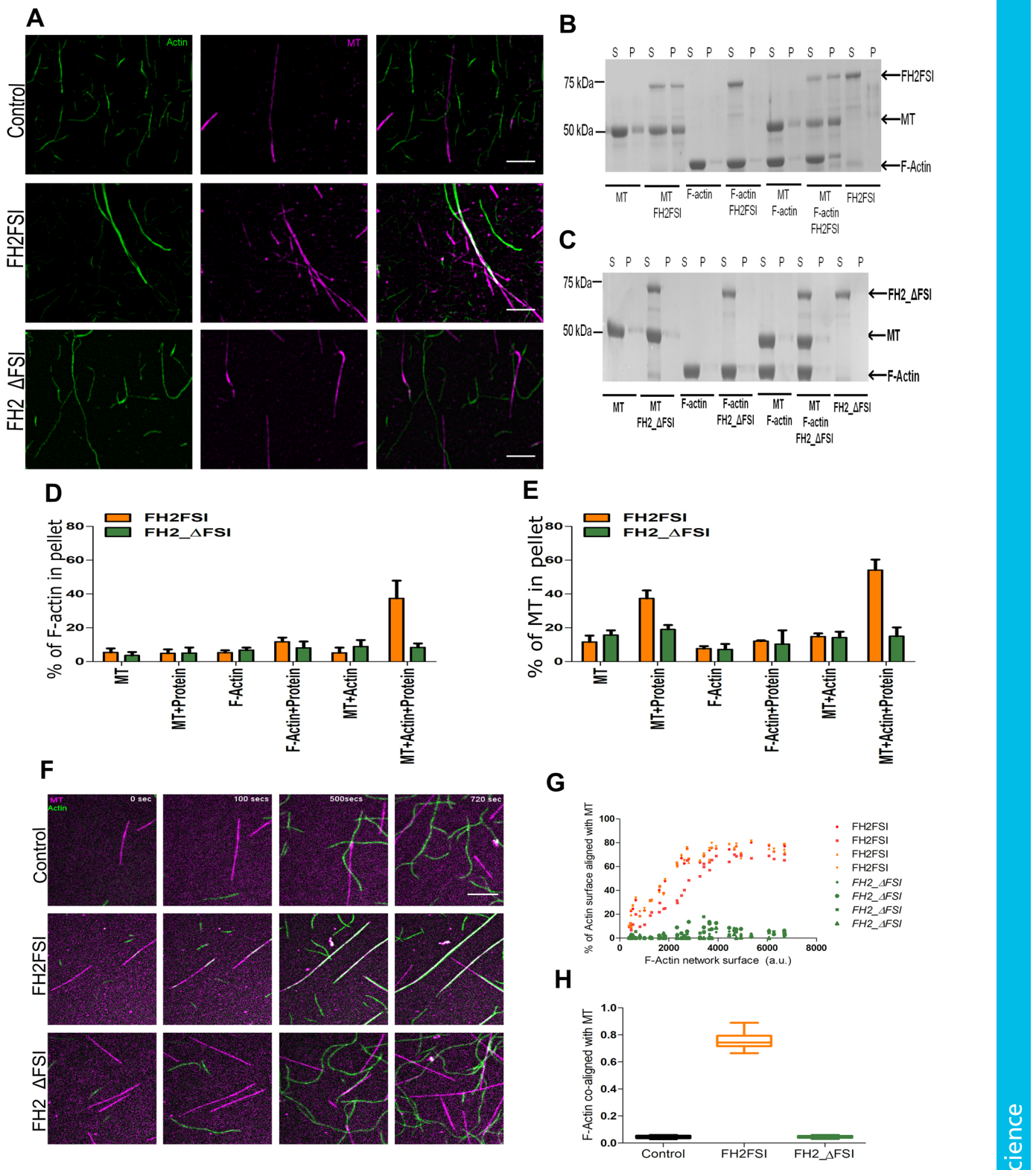

Fig. 5. See next page for legend.

We directly tested the F-actin–MT cross-bridging activity of Fmn2 using *in vitro* biochemistry and reconstitution strategies with purified recombinant Fmn2 fragments. These studies revealed that the Fmn2 homodimer is a potent actin–MT cross-linker, with its C-terminal FSI domain central to this function. The conserved FSI domain of the *Drosophila* orthologue of Fmn2, Capu, has been previously shown to interact with both F-actin and MTs via non-specific charge-based interactions (Roth-Johnson et al., 2014), and Capu has been implicated in actin–MT cross-linking in *Drosophila* oocytes (Dahlgaard et al., 2007; Rosales-Nieves et al., 2006). In neurons, expression of full-length Fmn2, but not FSI domain-deleted constructs, rescued the MT phenotypes associated with

Journal of Cell Science (2021) 134, jcs252916. doi:10.1242/jcs.252916

Fig. 5. The FSI domain of Fmn2 is required for efficient cross-linking of F-actin and MTs. (A) Visualization of the phalloidin-stabilized actin (left) and Taxol-stabilized MT (middle) cross-linking in the absence of purified protein (upper panels; control) or in the presence of FH2FSI (middle panels) or FH2-ΔFSI (lower panels). The reaction mixture was incubated with FH2FSI or FH2-ΔFSI for 30 mins before centrifugation followed by visualization. Right-hand panels show merge images of actin and MTs. Images are representative of three experiments. Scale bars: 5 µm. (B) Representative SDS–PAGE showing cross-linking of phalloidin-stabilized actin and Taxol-stabilized MT polymers by FH2FSI after incubation for 30 mins and centrifugation at 2000 ***g*** (S, supernatant; P, pellet). (C) Representative SDS–PAGE showing lack of cross-linking of the actin and MT complexes in the presence of FH2-ΔFSI after incubation for 30 mins and centrifugation at 2000 ***g***. (D) Quantification of the cross-linked phalloidin-stabilized actin in the presence of FH2FSI or FH2-ΔFSI from the co-sedimentation assays. The data represents the mean±s.d. from four independent experiments. (E) Quantification of the cross-linked Taxol-stabilized MTs in the presence of FH2FSI or FH2-ΔFSI from the co-sedimentation assays. The data represents the mean±s.d. from four independent experiments. (F) Representative frames from time-lapse TIRF imaging of co-polymerizing MTs and F-actin. In the control (upper panels), tubulin dimers (25 µM; magenta) were co-polymerized with actin monomers (1 µM; green). The filaments were distributed randomly without any association. Addition of FH2FSI (middle panels) caused the co-assembling MT and F-actin filaments to co-align and form thick hybrid bundles; however, addition of FH2-ΔFSI (lower panels) did not lead to alignment and cross-bridging of MTs and F-actin, and each of the individual filaments remained unassociated with each other and were distributed randomly. Images are representative of two independent experiments. Scale bar: 10 µm. (G) Percentage of F-actin co-aligned with MTs as a function of the F-actin network surface in the presence of FH2FSI or FH2-ΔFSI (four individual curves for each protein; a.u., arbitrary units). (H) Box plot analysis of the F-actin surface co-aligned with MTs in the presence of FH2FSI or FH2-ΔFSI (the graph represents the co-alignment at the end of 720 secs from 20 individual data sets for each condition). Boxes show the median interquartile range, with whiskers indicating the range.

Fmn2 depletion, underscoring the importance of this domain in microfilament–MT cross-linking.

Taken together, our data posits cross-linking activity as the central mechanism by which Fmn2 regulates MT dynamics in filopodia. It is possible that there are additional mechanisms involved. For example, Fmn2 depletion might result in filopodial F-actin becoming sparser, contributing to the observed phenotypes. A contrary argument is that a reduction in physical hindrance to MT advance should have reduced predisposition to MT catastrophe and not increased it. Furthermore, similar incursion depths of MTs in control and Fmn2-depleted filopodia also suggest mechanical hindrance to MT extension is unlikely to have been altered. However, our *in vitro* studies provide compelling support for the cross-bridging mechanism playing a significant role.

The FSI domain is the common interface between F-actin- and MT-binding, and it is also required for efficient actin nucleation and elongation by the FH2 domain (Vizcarra et al., 2014). Consequently, it is not possible to examine the effect of Fmn2 on actin and MT dynamics independently. *In vitro* studies suggest that MTs can inhibit actin nucleation by Capu, but do not influence activity when Capu is bound to the growing barbed ends of F-actin filaments (Roth-Johnson et al., 2014). We reason that the FSI domain is involved in supporting nucleation and/or elongation of F-actin when bound to the F-actin barbed end; however, we propose it is also capable of F-actin filament side binding via non-specific charge interactions. The latter activity could result in attenuated actin nucleation activity. When an invading MT reaches Fmn2-decorated filopodial F-actin bundles, one FSI domain of the Fmn2 dimer might attach to the polymerizing MT while the other FSI domain continues to interact with F-actin. This coupling could guide the MT into the filopodium and stabilize it from catastrophe (Fig. 7G). Growth cone

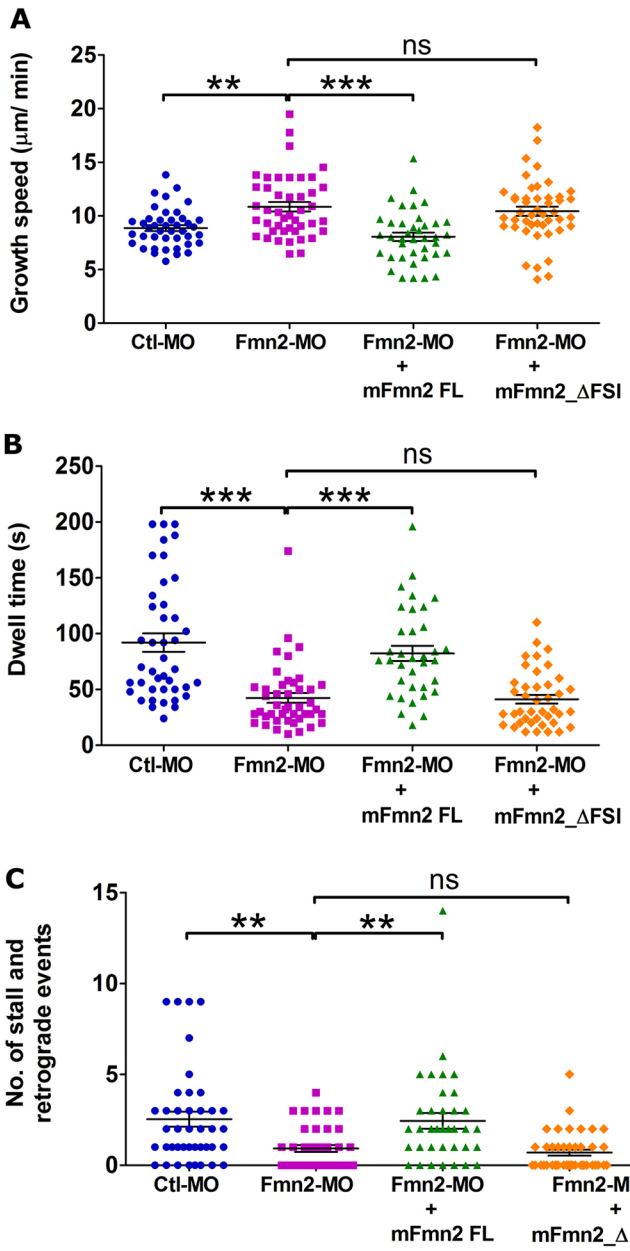

Fig. 6. The FSI domain of Fmn2 is required for coupling actin and MTs in filopodia. (A) Growth speed, (B) dwell time and (C) retrograde and pause events of EB3 comets in filopodia of Fmn2-MO-treated growth cones were rescued by morpholino-resistant full-length mouse Fmn2 (mFmn2) but not when the FSI domain was lacking (mFmn2-ΔFSI). Rescue was assessed by comparison with Fmn2-MO-treated growth cones. In A: Ctl-MO, *n*=42; Fmn2-MO, *n*=44; mFmn2-FL rescue, *n*=35; mFmn2-ΔFSI, *n*=41. In B: Ctl-MO, *n*=42; Fmn2-MO, *n*=44; mFmn2-FL rescue, *n*=39; mFmn2-ΔFSI, *n*=46. In C: Ctl-MO, *n*=41; Fmn2-MO, *n*=39; mFmn2-FL rescue, *n*=36; mFmn2-ΔFSI, *n*=43. The mean±s.e.m. is indicated, and the data shown are from more than three independent experiments. ***P<0.001; **P<0.01; ns, P>0.05 (Kruskal–Wallis test followed by Dunn's multiple comparison test).

turning involves selective stabilization of the chemosensory filopodia towards the direction of the turning (Zheng et al., 1996), which is facilitated by the increased capture of MTs within filopodia (Buck and Zheng, 2002; Mack et al., 2000; Sabry et al., 1991; Williamson et al., 1996). Stable MTs within filopodia ensure targeted cargo delivery and also enhance the mechanical resilience of the filopodia. Consistent with this model, we find that MT entry is associated with

Journal of Cell Science (2021) 134, jcs252916. doi:10.1242/jcs.252916

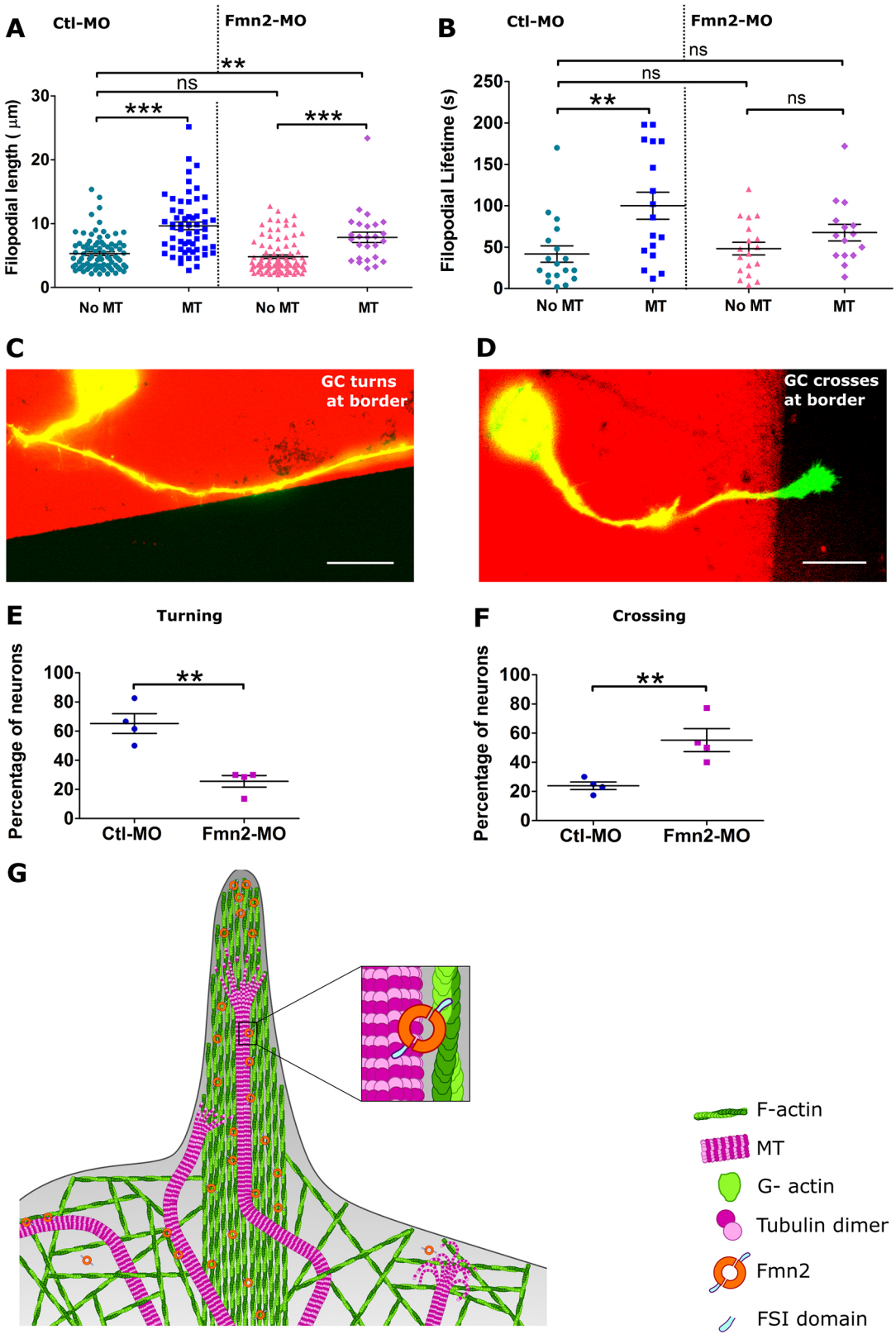

Fig. 7. See next page for legend.

longer filopodial lifetimes and lengths (Barzik et al., 2014; McNeely et al., 2017). As Fmn2 mediates the capture, incursion and lifetimes of MT inside filopodia, we find that depletion of Fmn2 results in deficits in growth cone turning at substrate boundaries.

Turning at substrate boundaries involves biased stabilization of the growth cone. This is regulated by a complicated interplay between actomyosin-dependent protrusion and modulation of adhesion properties, as well as the stabilization of filopodia by

Journal of Cell Science (2021) 134, jcs252916. doi:10.1242/jcs.252916

Fig. 7. Fmn2 is required for filopodial stability and growth cone turning *in vitro* and for MT stability *in vivo*. (A) Comparison of filopodial lengths with and without MTs inside from Ctl-MO- and Fmn2-MO-treated growth cones. Immunofluorescence was used to detect MTs, while fluorescently labelled phalloidin marked F-actin (Ctl-MO no MT, n=92; Ctl-MO MT, n=104; P=0.0047; Fmn2-MO no MT, n=83; Fmn2-MO MT, n=21; P=0.1584). (B) Comparison of filopodial lifetimes with or without EB3 entry during imaging for 100 frames with 2 s frame interval (Ctl-MO no MT, n=18; Ctl-MO MT, n=17; P<0.0001; Fmn2-MO no MT, n=18; Fmn2-MO MT, n=15; P<0.0001). Data points and the mean±s.e.m. are shown. ***P<0.001; **P<0.01; ns, P>0.05 (Kruskal–Wallis test followed by Dunn's multiple comparison test). (C) Representative image of a control neuron co-transfected with Ctl-MO and soluble GFP showing a growth cone turning at the border between laminin and fibronectin (L+FN; red) and poly-L-lysine (PLL; black) to continue to stay on the preferred L+FN region. (D) Representative image of an Fmn2-MO and GFP co-transfected growth cone failing to turn and crossing over from the L+FN side into the PLL region. Scale bars: 20 µm, Quantification of (E) turning (P=0.0016) and (F) crossing (P=0.0016) events of growth cones from the L+FN region encountering a border with PLL (Ctl-MO, n=68; Fmn2-MO, n=78; data compiled from four independent biological replicates; mean±s.e.m.). **P<0.01 (unpaired, two-tailed Student's t-test). (G) Schematic representation of a growth cone filopodium with parallel actin bundles showing MT incursion into the filopodium. Fmn2 dimers on filopodial F-actin bundles cross-bridge exploratory MTs resulting in co-alignment and targetting into filopodia. Inset shows the suggested model wherein one monomer of the Fmn2 dimer binds to F-actin and the other binds to the MT lattice. Fmn2-dependent cross-linking of MTs to F-actin in filopodia increases the stability of the invading MT. The filopodial lifetimes and stability are likely increased due to the stable MT providing a track for cargo delivery and increasing the mechanical resilience to the filopodium. It is proposed that biased stabilization of filopodia, in response to chemotactic and/or haptotactic cues results in growth cone turning.

MT capture. We have recently shown that Fmn2 also regulates a molecular clutch to generate traction forces in growth cones (Ghate et al., 2020). It is currently not possible to separate the contribution of these two Fmn2 functions in growth cone turning at substrate borders; however, a recent study implicates MT-dependent filopodial stabilization as the dominant component in growth cone advance (Turney et al., 2020 preprint).

Because mutation of Fmn2 is associated with intellectual disability, learning and memory deficits, and because the protein is localized to dendritic spines (Law et al., 2014), it will be of interest to examine the role of Fmn2-mediated actin–MT crosstalk in the context of structural plasticity of dendritic spines (Koganezawa et al., 2017; Merriam et al., 2013). Similarly, the enhanced dynamicity of MTs may have implications for axonal regrowth following injury (Blanquie and Bradke, 2018; Tang and Chisholm, 2016).

In oocytes, a Fmn2-dependent F-actin 'cage' is assembled around the MT spindle that is essential for spindle positioning and chromosome segregation (Azoury et al., 2008; Mogessie and Schuh, 2017). It is tempting to speculate that actin–MT crosstalk facilitated by Fmn2 may regulate the development of the F-actin 'cage' and also explain the reduction in kinetochore fibres in Fmn2$^{-/-}$ oocytes (Mogessie and Schuh, 2017).

In summary, this study identifies Fmn2 as a novel mediator of actin–MT crosstalk in neuronal growth cones and provides a mechanistic framework for uncovering neurodevelopmental functions of Fmn2. Our study underscores the importance of precise coordination between the actin and MT cytoskeletons in highly precise and adaptive processes like the chemotactic motility of cells.

MATERIALS AND METHODS

Plasmid constructs

Details of the sources and cloning of plasmids used in this study are listed in Table S1. Neurons were co-transfected with pCAG-GFP or pCAG-mCherry plasmids along with morpholinos to select for transfected growth cones. pCAG-EB3-GFP, pCAG-EB3-mCherry or pCS2-GFP-tubulin were used to visualize MT dynamics. *Ngn1*: EB3–GFP and *ngn1*: TagRFP–CAAX were used to label polymerizing MTs and label the membrane of zebrafish RB neurons. Rescue experiments were undertaken using pCAG-mFmn2-GFP and pCAG-mFmn2-ΔFSI-GFP. For expression of recombinant protein fragments in bacteria, chick Fmn2 FH2FSI (amino acids 1148–1587) and FH2-ΔFSI (amino acids 1148–1563) fragments were generated from full-length chick Fmn2 (GenBank: KU711529.1) and cloned into pGEX-6P1 vector (gift from Dr Thomas Pucadyil, IISER Pune).

Primary neuronal cultures and transfection

Freshly fertilized White Leghorn eggs were obtained from Venkateshwara Hatcheries Ltd., India. All protocols were followed in accordance with procedures approved by the Institutional Animal Ethics Committee, IISER Pune, India. Hamburger–Hamilton (HH) stage 25–26 embryos were dissected in a laminar flow hood, and spinal tissue between the fore and hind limbs was isolated. The tissue was dissociated using trypsin (0.25% trypsin in EDTA; Lonza) by incubation at 37°C for 15 min. The dissociated tissue was then electroporated (Sahasrabudhe et al., 2016) with suitable plasmid (5–20 µg) and/or morpholinos (100 µM) in Optimem (Gibco) medium, plated in culturing medium (L-15, 10% FBS and 1× penicillin-streptomycin; Gibco) and allowed to grow at 37°C without CO_2 for 24–36 h. Before plating, the glass coverslips were coated with 1 mg/ml poly-L-lysine (PLL; Sigma) and 20 µg/ml laminin (Sigma).

Morpholino-based knockdown

To knockdown Fmn2 in chick neurons, an anti-Fmn2 translation-blocking morpholino (5′-CCATCTTGATTCCCCATGATTTTTC-3′) were used along with a non-specific morpholino as a negative control (5′-CCTCT-TACCTCAGTTACAATTTATA-3′). Previously, we have characterized this and other morpholino sequences and demonstrated effective and specific knockdown of Fmn2 protein expression in chick spinal commissural neurons (Sahasrabudhe et al., 2016). This was established using immunoblot and immunofluorescence analyses employing antibodies against endogenous chick Fmn2. In this study, we report greater than 75% knockdown of endogenous protein in growth cones of spinal neurons, using immunofluorescence (Fig. S1A). In these experiments, pCAG-GFP plasmid was co-transfected along with morpholinos and incubated for 36 h before immunostaining with anti-Fmn2 (Sahasrabudhe et al., 2016). Only GFP-expressing neurons were considered for analysis. Fmn2 fluorescence was normalized to growth cone area.

Specificity of this morpholino has been established by rescuing the knockdown phenotypes through the co-expression of morpholino-resistant Fmn2 cDNA in primary neurons (this study and Sahasrabudhe et al., 2016) and *in vivo* (Sahasrabudhe et al., 2016).

Immunofluorescence

Neurons were cultured for 24 h before fixing. For STED and detyrosinated: total tubulin ratio imaging, staining was performed according to a procedure presented previously (Biswas and Kalil, 2018). Briefly, the cultures were pre-extracted for 90 s with 0.4% glutaraldehyde and 0.2% Triton X-100 in PHEM buffer (60 mM PIPES, 25 mM HEPES, 10 mM EGTA and 4 mM $MgSO_4{\cdot}7H_2O$; all sourced from Sigma) and then fixed in 3% glutaraldehyde (in PHEM buffer) for 15 min at 37°C. After washes with 0.5% BSA in 1× phosphate-buffered saline (PBS), permeabilization was performed using 0.5% Triton X-100 for 10 min at room temperature. Glutaraldehyde was quenched with 5 mg/ml sodium borohydride for 5 min in 1× PBS. Blocking buffer (10% BSA) was used for 1 h. Primary antibody incubation was performed overnight at 4°C, followed by secondary antibody incubation for 1 h at room temperature. The samples were then mounted in Mowiol–DABCO medium [2.5% 1,4-diazabiocyclo-octane (DABCO), 10% Mowiol 4-88, 25% glycerol and 0.1 M Tris-HCL, pH 8.5; all sourced from Sigma]. For triple antibody staining of Fmn2, MTs and actin, the neurons were fixed using 4% paraformaldehyde and 0.05% glutaraldehyde in PHEM buffer for 20 min at room temperature. The neurons were permeabilized using 0.01% Triton X-100 for 10 min. Incubation with primary antibody was performed in blocking buffer (3% BSA in PHEM buffer) at 4°C overnight. Secondary

antibody incubation was for 1 h before mounting in 80% glycerol. All the washes were performed in PHEM buffer. The primary antibodies for staining total MTs (anti-α-tubulin; DM1a; Sigma) and detyrosinated tubulin (EMD Millipore; AB3201) were used at 1:3000 and 1:500 dilution, respectively. The anti-Fmn2 antibody was generated in house (Sahasrabudhe et al., 2016) and was used at 1:200 dilution. Secondary antibodies from Invitrogen, namely Alexa Fluor 568-conjugated goat anti-mouse IgG and Alexa Fluor 405-conjugated goat anti-mouse IgG (for total MT), were used at 1:1000 dilution. Alexa Fluor 488-conjugated goat anti-rabbit IgG (for detyrosinated MTs and Fmn2; Invitrogen) was used at 1:500 dilution. F-actin was visualized using Alexa Fluor 633–phalloidin and Alexa Fluor 568–phalloidin (Invitrogen) at 1:100 and 1:1000 dilution, respectively. The samples were mounted in Mowiol–DABCO medium.

STED nanoscopy and analysis

For STED nanoscopy, a Leica TCS SP8 STED microscope with 100×, 1.4 NA PL APO oil objective was used to image growth cones. MTs labelled with Alexa Fluor 568 were depleted using a continuous wave (CW) 660 nm depletion laser. F-actin labelled with phalloidin–Alexa Fluor 633 was depleted using a 775 nm CW laser. Images were acquired using a HyD detector with 0.5–6 ns time gating and a pixel size of <36 nm. Images were deconvolved using the default settings and 15 iterations of the CMLE JM algorithm in the Huygens software (version 17.04.0p6 64b; Scientific Volume Imaging).

Neurons chosen for imaging were identified by the expression of a co-transfected soluble GFP plasmid construct. Any protrusion from the growth cone equal to or longer than 2 µm was considered for filopodia analysis. The number and length of filopodia were measured manually using the line tool in the ImageJ software (NIH, Bethesda, MD). Analysis of alignment between MTs and actin was done using the phalloidin channel as a reference to identify the initial position of alignment of the MT with F-actin, and the length of alignment was measured by tracking the MT along the actin bundle using the segmented line tool in ImageJ. For MT entry into filopodia, a minimum incursion of 0.5 µm from the base of filopodia was considered for analysis.

Imaging and analysis of detyrosinated and total microtubules in the growth cone

For confocal imaging, a Zeiss 780 LSM system was used with a 63×/1.4 NA Plan-Apochromat oil objective. The images were acquired using a 405 nm diode laser (for total MTs), a 488 nm argon laser (for detyrosinated MTs or Fmn2) and a 561 nm DPSS laser (for Alexa Fluor 568–phalloidin) for excitation with appropriate zoom to maintain a pixel size of ∼100 nm.

For intensity measurements, imaging was conducted maintaining the same parameters across control and Fmn2-MO-treated samples. The total MT image was thresholded (Otsu method) using ImageJ and was used as a mask to measure the intensity of detyrosinated tubulin. The fluorescence was quantified using the formula: corrected fluorescence=integrated density−(area of selected cell×mean background fluorescence). The detyrosinated tubulin intensity was normalized to total tubulin intensity in the growth cone.

Live-cell imaging of primary neurons

Growth cones were grown *in vitro* for 24 h or 36 h (rescue experiments). 5 µg of plasmid was used for transfection along with morpholino treatment. Only neurons with moderate expression levels were considered for imaging and analysis. Live imaging of both EB3–GFP and EB3–mCherry (for rescue and Blebbistatin experiments, respectively) were done on an IX81 system (Olympus Corporation) equipped with a Hamamatsu ORCA-R2 CCD camera using a 100×, NA 1.4 Plan Apo oil immersion objective. 30 µM of Blebbistatin (− enantiomer; Sigma) was added in the culture medium. Imaging commenced 15 min after the addition of Blebbistatin. Wide-field imaging was performed using the Xcellence RT (Olympus Corporation) software for 100 frames with a time interval of 2 s between each frame. During imaging, the cultures were maintained at a constant temperature of 37°C.

EB3 comet tracking and data analysis

Comet tracking for the whole growth cone analysis was performed using plusTipTracker 1.1.4 (Applegate et al., 2011; Matov et al., 2010) and MATLAB 2010b (Mathworks). The images were first background subtracted in ImageJ using a rolling ball radius of 50 pixels, to enhance the contrast. Detection of the comet was done via the plusTipGetTracks graphical user interface (GUI) with the following settings (Biswas and Kalil, 2018; Stout et al., 2014): detection method=anisotropic gaussian; PSF sigma=1–1.5; and alpha value=0.005–0.02, depending on the most faithful detection of comets across several frames of each movie. Tracking of the comets was performed using the following parameters: search radius (range)=3–12; minimum sub-track length (frames)=3; break non-linear tracks was unchecked; maximum gap length (frames)=11; maximum shrinkage factor (relative to growth speed)=0.8; maximum angle (degrees) forward=40, backward=20; fluctuation radius=3.5. The post-processing parameters used were frame rate (s)=2 and pixel size (nm)=64. Raw values of growth speed, growth length, growth lifetime and dynamicity (collective displacement of all gap-containing tracks over the collective lifetimes) were exported to Graph Pad Prism 5 and used for graphical representation and analysis. Growth speed of comet tracks was visualized using the growth speed range from 0 to 20 µm/min in all frames using the plusTipSeeTracks GUI.

The EB3 comet tracking in the filopodia was conducted manually to avoid any false detection due to movement of the filopodia itself. Comets that emerged from the MT-dense region were tracked using the point tool of ImageJ, from the central domain to the peripheral or filopodial region, if they appeared in at least three continuous frames. The coordinates of the comet position were saved as regions of interest (ROIs) and exported to Microsoft Excel for calculation of growth speeds. Comets that disappeared were observed for a minimum of three continuous frames to check for rescue. Only unambiguous comet entries into filopodia were considered for dwell-time analysis. Comets entering the filopodia were manually tracked for growth speed and excursion depth analysis. The number of comets in each frame of the movie was extracted from the 'movieinfo' file generated by plusTipTracker using the following code written in MATLAB:

```
a=[100,1];
for i=1:100
a(i,1)=(length(movieInfo(i,1).xCoord));
end
```

The median value of comet numbers obtained from 100 frames of each movie was normalized to the area of the growth cone. The area of the growth cone was a mean of ten measurements obtained manually using the freehand selection tool of ImageJ for every tenth frame.

Protein purification

Actin was purified from rabbit muscle powder (prepared as described in Pardee and Spudich, 1982) following standard protocols (Pollard, 1984) and labelled with Alexa Fluor 488–maleimide (Hansen et al., 2013). Porcine brain tubulin and rhodamine-labelled tubulin were purchased from Cytoskeleton Inc. (cat. no. T240A and TL590M-A, respectively). Bovine brain tubulin was used for dynamic colocalization studies of actin and MTs using TIRF microscopy. The GST-tagged chick Fmn2 constructs were expressed in BL21 Rosetta cells by inducing with 0.4 mM IPTG and were purified following standard protocols (Harris and Higgs, 2006) using glutathione beads and further stored at 4°C in $HEKG_5$ (20 mM HEPES, 1 mM EDTA, 50 mM KCl and 5% glycerol) buffer. The human DAAM1 fragment was purified as described previously (Dutta et al., 2017).

Actin nucleation assay

A 12 µM rabbit muscle actin (RMA) stock was prepared in a tube using 10% pyrene-labelled actin and 90% unlabelled actin. A 10 µl volume of this mixture was incubated for 2 min at room temperature with 4.2 µl of exchange buffer (1 mM $MgCl_2$ and 10 mM EGTA). G-buffer [10 mM Tris-HCl pH 8.0, 0.2 mM dithiothreitol (DTT), 0.2 mM ATP and 0.2 mM $CaCl_2$] was added to the above reaction mix. Different concentrations of the desired protein (final protein concentrations are mentioned in the figure legends) were added, and the volume was adjusted with $HEKG_5$ buffer. To start the polymerization reaction, 20× initiation mix (1 M KCl, 40 mM $MgCl_2$ and 10 mM ATP) was added. The actin nucleation was measured from the

fluorescence of pyrene–actin at 365 nm (excitation) and 407 nm (emission) wavelengths at 25°C using a fluorescence spectrophotometer (QM40, Photon Technology International, Lawrenceville, NJ; and Fluoromax, Horiba) (Moseley et al., 2006).

Fmn2 interactions with F-actin or microtubules

Phalloidin-stabilized F-actin was prepared from 30 µM G-actin by incubating actin with F-buffer (10 mM Tris-HCl pH 8.0, 0.2 mM $CaCl_2$, 0.2 mM DTT, 2 mM $MgCl_2$, 0.7 mM ATP and 50 mM KCl) for 1 h at room temperature. Then, 2 µM of Fmn2 FH2FSI or FH2-ΔFSI was incubated with increasing concentration of stabilized F-actin for another 30 mins. For binding experiments evaluating the dependence on salt concentrations, phalloidin-stabilized F-actin was incubated with 2 µM of Fmn2 FH2FSI in F-buffer (10 mM Tris-HCl pH 7.5, 0.2 mM $CaCl_2$, 0.2 mM DTT, 2 mM $MgCl_2$, 0.7 mM ATP and varying salt concentrations – 0 mM, 50 mM, 100 mM and 150 mM KCl) for 30 mins at room temperature. Samples were centrifuged for 20 mins at 320,000 ***g*** and analysed using SDS–PAGE. The amount of protein bound to actin in the pellet was quantified by densitometry on Coomassie-stained gels using ImageJ software (version 1.52 g). The amount of protein bound to F-actin was plotted versus F-actin concentrations, and the apparent dissociation constant was calculated by fitting a non-linear regression hyperbolic curve in Graph Pad Prism 5.0 software using the equation $Y=B_{max}\times X/(K_D+X)$, where B_{max} is the maximum specific binding, having the same units as Y. K_D is denoted as the equilibrium binding constant, having the same units as X, and is the ligand concentration needed to achieve a half-maximum binding at equilibrium. In absence of filamentous actin, no protein was detected in the pellet, which signified the solubility of the protein. To determine the affinity of MTs to Fmn2, 100 µM tubulin was polymerized at 37°C in BRB 80 (80 mM PIPES pH 6.9, 1 mM EGTA and 1 mM $MgCl_2$) buffer with 1 mM GTP for 1 h. To stabilize the MTs, we used 20 µM Taxol (Cytoskeleton Inc.). Proteins at 2 µM were incubated with the Taxol-stabilized MTs for another 1 h at room temperature. For binding experiments evaluating the dependence on salt concentrations, Taxol-stabilized MTs were incubated with 2 µM Fmn2 FH2FSI in BRB 80 (80 mM PIPES pH 7.5, 1 mM EGTA and 1 mM $MgCl_2$) buffer with 1 mM GTP and varying concentrations of salt (0 mM, 50 mM, 100 mM and 150 mM KCl) for 1 h at room temperature. Samples were centrifuged for 20 min at 100,000 ***g*** and analysed using SDS–PAGE. The amount of protein bound to MTs was quantified as described above.

Actin and microtubule bundling assays

Increasing concentrations of protein (FH2FSI and FH2-ΔFSI) were added to 2 µM pre-formed F-actin and allowed to form F-actin bundles in the presence of F-buffer. The amount of bundle formation was quantified after 30 min of incubation and centrifugation at 10,000 ***g*** for 10 min to selectively pellet bundled F-actin. In the F-actin control, the actin remained in the supernatant. The amount of actin fraction in the pellet and supernatant was quantified by densitometry of Coomassie-stained gels using the ImageJ software. The percentage of the actin in the pellet was calculated from the amount of actin in the pellet divided by the total amount of actin in the supernatant and pellet. The percentage of actin in the pellet was plotted against the increasing concentration of the protein using Graph Pad Prism 5.0 software.

In the MT bundling assay, 2 µM pre-formed MTs were incubated with increasing concentrations of the protein (FH2FSI and FH2-ΔFSI) for 30 min and centrifuged at 5000 ***g*** for 10 min. The amount of the MT fraction in the pellet and supernatant was quantified by densitometry of Coomassie-stained gels using the ImageJ software. The percentage of MTs in the pellet was calculated and plotted in a similar manner as described above for actin pellets.

Microtubule stabilization assay

MTs were polymerized from 100 µM tubulin in the presence of BRB 80 buffer (80 mM PIPES, 1 mM EGTA and 1 mM $MgCl_2$) with 1 mM GTP for 1 h. To stabilize the MTs, we used 20 µM Taxol. Increasing concentrations of FH2FSI were incubated with the MTs for 30 min at room temperature. To assess the MT stability upon cold-induced depolymerization in the presence of FH2FSI, the samples containing MTs and FH2FSI, and the respective control samples, were incubated on ice for another 30 min and spun in a bench-top ultracentrifuge (TLA 100.3; Beckman Coulter) for 20 min at 100,000 ***g*** at 4°C to isolate cold-stable MTs. Supernatant and pellets were resolved on a 10% SDS–PAGE gel, and the proteins were detected by Coomassie staining.

Cross-linking of F-actin and microtubules

Phalloidin-stabilized actin filaments were generated from G-actin in the presence of F-buffer. Taxol-stabilized MTs were generated from tubulin in the presence of BRB 80 buffer. 2 µM pre-formed phalloidin-stabilized actin and 2 µM Taxol-stabilized MTs were mixed in the presence of BRB 80 buffer and incubated for 30 min with 2 µM purified FH2FSI or 2 µM FH2-ΔFSI protein. The mixture was centrifuged at 2000 ***g*** for 10 min. Supernatants and pellets were analysed using SDS–PAGE. The amount of F-actin and MTs in the pellet was quantified separately, following the method described above.

TIRF microscopy and evaluation of concomitant microtubule and actin assembly

Perfusion chambers were prepared from glass slides and coverslips using double-sided sticky tape, and the chambers were coated with silane–PEG (Creative works) following standard protocols (Portran et al., 2013). Alexa Fluor 488–phalloidin-labelled F-actin, in the absence or presence of either FH2FSI or FH2-ΔFSI, was imaged using an inverted microscope (ApoN/TIRF 100×/1.49 oil immersion objective on an IX 81 system; Olympus) equipped with a Cell TIRF module (Olympus) and a Hamamatsu ORCA-R2 CCD camera in TIRF buffer (0.2% methylcellulose, 3 mg/ml glucose, 20 µg/ml catalase and 100 µg/ml glucose oxidase). To observe the MT bundles under the TIRF microscope, 5% rhodamine-labelled tubulin and 95% unlabelled tubulin was used to form Taxol-stabilized MTs and incubated with the protein (either FH2FSI or FH2-ΔFSI). Co-alignment of preformed F-actin and Taxol-stabilized MTs, in the presence or absence of either FH2FSI or FH2-ΔFSI, was also imaged similarly using the TIRF mode of an Olympus IX 81 microscope.

Actin and MT growth inside the perfusion chamber was initiated by flowing 1 µM actin monomers (12% Alexa Fluor 488-labelled G-actin), 25 µM tubulin dimers (10% ATTO-565-labelled tubulin) and labelled MT seeds in the absence or presence of 0.5 µM FH2FSI or FH2-ΔFSI. The buffer used for the reaction contained 10 mM HEPES, 50 mM KCl, 5 mM $MgCl_2$, 1 mM EGTA, 20 mM DTT, 1% BSA and 0.1 mM ATP along with the TIRF buffer. Samples were visualized using a TIRF microscope (Eclipse Ti, Nikon with an iLAS TIRF system) equipped with a EMCCD camera (Evolve 512, Photometrics) and controlled using Metamorph software (Molecular Devices). The actin and MT samples were observed using an Apochromat 100×/1.49 oil immersion objective. Simultaneous dual-colour time-lapse imaging was performed at 35°C for actin and tubulin co-assembly using a dual emission splitter. Images were acquired for 12 min at 1 frame per 20 secs with 100 ms exposure time. All image analysis was conducted using ImageJ software and a custom written co-alignment analysis macro (Prezel et al., 2017).

Microcontact printing and substrate-choice border assay

Polydimethylsiloxane (PDMS) stamps containing a zig-zag pattern of 100 or 150 µm-wide stripes with a height of 10 µm were made from a silicon master (custom manufactured by Bonda Technology Pte. Ltd., Singapore). The silicon wafer was silanized with trichloromethylsilane vapours in vacuum for 5 min. After keeping the master in the vacuum desiccator overnight, the process was completed by heating the master plate at 70°C for 30 min. A 10:1 mixture of PDMS and curing agent was degassed by centrifugation at 1240 ***g*** for 5 min. The mixture was poured onto the silicon master and cured at 60°C for 2 h. Microcontact printing on glass coverslips was performed using protocol adapted from Thery and Piel (2009). The stamps were inked with 100 µl of a solution of tetramethylrhodamine (TMR)–BSA (2.5 µg/ml), laminin (10 µg/ml) and fibronectin (10 µg/ml) for 20 min at room temperature. After removing the excess solution, the stamps were washed with 1× PBS and allowed to dry for a minute before

printing onto the PLL-coated (0.1 mg/ml) glass coverslips. PBS was added to prevent drying of the pattern on the 35 mm glass-bottomed dish.

Alternating borders of poly-L-lysine and ECM proteins were created by the microcontact printing method described above. Neurons co-transfected with a soluble GFP-expressing plasmid along with control or Fmn2 morpholinos were grown on the patterned substrates for 36 h before imaging. Only neurons whose cell bodies were on the laminin and fibronectin patterns (visible as red stripes due to the presence of TMR–BSA) and whose axons approached the borders were considered for analysis. Imaging was done using a 40×/1.4 NA oil objective on an Olympus IX81 microscope, and dual-channel (GFP and TMR) images were captured. Data were pooled from four independent biological replicates.

In vivo imaging and analysis of EB3 comets in zebrafish embryos

All procedures employed were approved by the Institutional Animal Ethics Committee (IAEC) of IISER Pune, India. Wild-type TU strain zebrafish maintained at 28.5°C under a 14 h light and 10 h dark cycle, housed in a recirculating aquarium (Techniplast) were crossed to obtain eggs. The eggs were co-injected with 25 pg *ngn1*: EB3–GFP, 25 pg *ngn1*: TagRFP–CAAX plasmids (both gifts from Dr Mary Halloran, University of Wisconsin, Madison, USA) and 0.125 mM morpholino (Gene Tools, LLC) in a 2 nl volume in the cytoplasm at the one-cell stage. The embryos were maintained at 28.5°C in E3 medium (5 mM NaCl, 0.17 mM KCl, 0.33 mM $MgSO_4$ and 0.33 mM $CaCl_2$) containing 0.002% Methylene Blue until the time of imaging.

For depleting Fmn2 levels *in vivo*, the splice-blocking Fmn2 morpholino (Zf-Fmn2-MO) used was 5′-ACAGAAGCGGTCATTACTTTTGGT-3′ and the standard control morpholino (Ctl-MO) used was 5′-CCTCTTACCTCAGTTACAATTTATA-3′. Zf-Fmn2-MO is expected to block the splicing of the intron between exons 5 and 6, resulting in the introduction of an early stop codon and an increase in size of the mRNA. The efficacy of the Zf-Fmn2-MO was evaluated using RT-PCR (Fig. S2B). The injected embryos were screened for mosaic expression of GFP and RFP, dechorionated and mounted laterally. Vacuum grease (Dow Corning) was used to make a well on the glass slide wherein the zebrafish embryo was positioned laterally in E3 medium containing 2% methylcellulose (Sigma Aldrich) and 0.03% MS-222 (Sigma Aldrich), then sealed with a coverslip. Growth cones of Rohon–Beard (RB) sensory neurons labelled by the *ngn* promoter-driven EB3–GFP and Tag–RFP in 24–28 hpf embryos were imaged on a Zeiss LSM 780 confocal microscope using a 63×/1.4 NA oil immersion objective for 100 frames, with 1.5 or 2 s intervals between frames. For analysis of EB3 comets obtained from *in vivo* imaging in zebrafish, kymographs were generated using the segmented line tool and KymographBuilder in ImageJ, and velocities and lifetimes were extracted using the velocity measurement tool.

Graphical representation and statistical analysis

All the graphical representation and statistical analyses were performed using GraphPad Prism 5. In the text, values are given as mean±s.e.m. Graphical representations are scatter dot plots, with the longer middle line indicating the mean and error bars indicating the s.e.m. For box plots, the box extends from the 25th to 75th percentiles, the line inside the box is plotted at the median and the whiskers represent the smallest and largest values. Column graphs represent means, and the error bars represent the s.d., unless otherwise indicated. The number of data points quantified in each graph is indicated either in the relevant text or figure legends. The sample sizes were based on the typical number of replicates used in similar studies. Mann–Whitney U test was employed for comparing two groups. When comparing more than two groups, Kruskal–Wallis test was used followed by Dunn's multiple comparison post-test.

Acknowledgements

The authors are grateful to Dr Laurent Blanchoin (CytomorphoLab, Université Grenoble-Alpes/CEA/CNRS/INRA, Grenoble, France) for hosting P.D. and providing technical expertise in establishing the TIRF-based actin and microtubule co-polymerization assays. Jérémie Gaillard and Christophe Gurein in the Blanchoin laboratory are acknowledged for providing purified bovine tubulin and rabbit skeletal muscle actin. The authors thank Dr G. Deshpande, Princeton University; Dr L. Blanchoin, Université Grenoble-Alpes/CEA/CNRS/INRA, Grenoble; Dr S. Rath, IISER Pune; and Dr N. K. Subhedar, IISER Pune for their critical reading of the manuscript. Preliminary biochemical experiments were conducted with goat tubulin provided by Kunalika Jain and Dr Chaitanya Athale, IISER Pune. The authors acknowledge the IISER Pune Microscopy Facility and the National Facility for Gene Function in Health and Disease (NFGFHD) at IISER Pune for access to equipment and infrastructure.

Competing interests

The authors declare no competing or financial interests.

Author contributions

Conceptualization: T.K., P.D., A.G.; Methodology: T.K., P.D., A.G.; Formal analysis: T.K., P.D., D.N., A.G.; Investigation: T.K., P.D., D.N.; Resources: S.M.; Writing - original draft: T.K., P.D., A.G.; Writing - review & editing: T.K., P.D., A.G.; Supervision: A.G.; Project administration: A.G.; Funding acquisition: A.G.

Funding

The study was supported from grants from the Department of Biotechnology, Ministry of Science and Technology, India (BT/PR12698/BRB/10/717/2009), Council of Scientific and Industrial Research, India [37(1689)/17/EMR-II] and intramural support from Indian Institute of Science Education and Research Pune to A.G. T.K. was supported by a University Grants Commission fellowship. P.D. was supported by a Research Associate fellowship from the Department of Biotechnology, Ministry of Science and Technology, India and an INSPIRE fellowship from the Department of Science and Technology, Ministry of Science and Technology, India (DST/INSPIRE/04/2017/001906). P.D. also received an EMBO Short Term fellowship to conduct experiments in the laboratory of Dr L. Blanchoin, Grenoble, France. D.N. is supported by a fellowship from the Council of Scientific and Industrial Research, India. The National Facility for Gene Function in Health and Disease (NFGFHD) at IISER Pune is supported by the Department of Biotechnology, Ministry of Science and Technology, India (BT/INF/22/SP17358/2016).

Peer review history

The peer review history is available online at https://journals.biologists.com/jcs/article-lookup/doi/10.1242/jcs.252916

References

Agís-Balboa, R. C., Pinheiro, P. S., Rebola, N., Kerimoglu, C., Benito, E., Gertig, M., Bahari-Javan, S., Jain, G., Burkhardt, S., Delalle, I. et al. (2017). Formin 2 links neuropsychiatric phenotypes at young age to an increased risk for dementia. *EMBO J.* **36**, 2815-2828. doi:10.15252/embj.201796821

Almuqbil, M., Hamdan, F. F., Mathonnet, G., Rosenblatt, B. and Srour, M. (2013). De novo deletion of FMN2 in a girl with mild non-syndromic intellectual disability. *Eur. J. Med. Genet.* **56**, 686-688. doi:10.1016/j.ejmg.2013.10.003

Applegate, K. T., Besson, S., Matov, A., Bagonis, M. H., Jaqaman, K. and Danuser, G. (2011). plusTipTracker: quantitative image analysis software for the measurement of microtubule dynamics. *J. Struct. Biol.* **176**, 168-184. doi:10.1016/j.jsb.2011.07.009

Azoury, J., Lee, K. W., Georget, V., Rassinier, P., Leader, B. and Verlhac, M. H. (2008). Spindle positioning in mouse oocytes relies on a dynamic meshwork of actin filaments. *Curr. Biol.* **18**, 1514-1519. doi:10.1016/j.cub.2008.08.044

Barzik, M., McClain, L. M., Gupton, S. L. and Gertler, F. B. (2014). Ena/VASP regulates mDia2-initiated filopodial length, dynamics, and function. *Mol. Biol. Cell* **25**, 2604-2619. doi:10.1091/mbc.e14-02-0712

Biswas, S. and Kalil, K. (2018). The microtubule-associated protein Tau mediates the organization of microtubules and their dynamic exploration of actin-rich Lamellipodia and Filopodia of cortical growth cones. *J. Neurosci.* **38**, 291-307. doi:10.1523/JNEUROSCI.2281-17.2017

Blanquie, O. and Bradke, F. (2018). Cytoskeleton dynamics in axon regeneration. *Curr. Opin Neurobiol.* **51**, 60-69. doi:10.1016/j.conb.2018.02.024

Buck, K. B. and Zheng, J. Q. (2002). Growth cone turning induced by direct local modification of microtubule dynamics. *J. Neurosci.* **22**, 9358-9367. doi:10.1523/JNEUROSCI.22-21-09358.2002

Coles, C. H. and Bradke, F. (2015). Coordinating neuronal actin-microtubule dynamics. *Curr. Biol.* **25**, R677-R691. doi:10.1016/j.cub.2015.06.020

Dahlgaard, K., Raposo, A. A. S. F., Niccoli, T. and St Johnston, D. (2007). Capu and Spire assemble a cytoplasmic actin mesh that maintains microtubule organization in the *Drosophila* oocyte. *Dev. Cell* **13**, 539-553. doi:10.1016/j.devcel.2007.09.003

Dillman, J. F., III, Dabney, L. P. and Pfister, K. K. (1996). Cytoplasmic dynein is associated with slow axonal transport. *Proc. Natl. Acad. Sci. USA* **93**, 141-144. doi:10.1073/pnas.93.1.141

Dogterom, M. and Koenderink, G. H. (2019). Actin-microtubule crosstalk in cell biology. *Nat. Rev. Mol. Cell Biol.* **20**, 38-54. doi:10.1038/s41580-018-0067-1
Dutta, P. and Maiti, S. (2015). Expression of multiple formins in adult tissues and during developmental stages of mouse brain. *Gene Expr. Patterns* **19**, 52-59. doi:10.1016/j.gep.2015.07.003
Dutta, P., Das, S. and Maiti, S. (2017). Non diaphanous formin delphilin acts as a barbed end capping protein. *Exp. Cell Res.* **357**, 163-169. doi:10.1016/j.yexcr.2017.05.014
Ghate, K., Mutalik, S. P., Sthanam, L. K., Sen, S. and Ghose, A. (2020). Fmn2 regulates growth cone motility by mediating a molecular clutch to generate traction forces. *Neuroscience* **448**, 160-171. doi:10.1016/j.neuroscience.2020.09.046
Guha, S., Patil, A., Muralidharan, H. and Baas, P. W. (2021). Mini-review: microtubule sliding in neurons. *Neurosci. Lett.* **753**, 135867. doi:10.1016/j.neulet.2021.135867
Hansen, S. D., Zuchero, J. B. and Mullins, R. D. (2013). Cytoplasmic actin: purification and single molecule assembly assays. *Methods Mol. Biol.* **1046**, 145-170. doi:10.1007/978-1-62703-538-5_9
Harris, E. S. and Higgs, H. N. (2006). Biochemical analysis of mammalian formin effects on actin dynamics. *Methods Enzymol.* **406**, 190-214. doi:10.1016/S0076-6879(06)06015-0
Henty-Ridilla, J. L., Rankova, A., Eskin, J. A., Kenny, K. and Goode, B. L. (2016). Accelerated actin filament polymerization from microtubule plus ends. *Science* **352**, 1004-1009. doi:10.1126/science.aaf1709
Hu, J., Bai, X., Bowen, J. R., Dolat, L., Korobova, F., Yu, W., Baas, P. W., Svitkina, T., Gallo, G. and Spiliotis, E. T. (2012). Septin-driven coordination of actin and microtubule remodeling regulates the collateral branching of axons. *Curr. Biol.* **22**, 1109-1115. doi:10.1016/j.cub.2012.04.019
Jean, D. C., Baas, P. W. and Black, M. M. (2012). A novel role for doublecortin and doublecortin-like kinase in regulating growth cone microtubules. *Hum. Mol. Genet.* **21**, 5511-5527. doi:10.1093/hmg/dds395
Koganezawa, N., Hanamura, K., Sekino, Y. and Shirao, T. (2017). The role of drebrin in dendritic spines. *Mol. Cell Neurosci.* **84**, 85-92. doi:10.1016/j.mcn.2017.01.004
Krainer, E. C., Ouderkirk, J. L., Miller, E. W., Miller, M. R., Mersich, A. T. and Blystone, S. D. (2013). The multiplicity of human formins: expression patterns in cells and tissues. *Cytoskeleton* **70**, 424-438. doi:10.1002/cm.21113
Kwon, S., Shin, H. and Lim, H. J. (2011). Dynamic interaction of formin proteins and cytoskeleton in mouse oocytes during meiotic maturation. *Mol. Hum. Reprod.* **17**, 317-327. doi:10.1093/molehr/gaq088
Law, R., Dixon-Salazar, T., Jerber, J., Cai, N., Abbasi, A. A., Zaki, M. S., Mittal, K., Gabriel, S. B., Rafiq, M. A., Khan, V. et al. (2014). Biallelic truncating mutations in FMN2, encoding the actin-regulatory protein Formin 2, cause nonsyndromic autosomal-recessive intellectual disability. *Am. J. Hum. Genet.* **95**, 721-728. doi:10.1016/j.ajhg.2014.10.016
Leader, B. and Leder, P. (2000). Formin-2, a novel formin homology protein of the cappuccino subfamily, is highly expressed in the developing and adult central nervous system. *Mech. Dev.* **93**, 221-231. doi:10.1016/S0925-4773(00)00276-8
Liu, M., Nadar, V. C., Kozielski, F., Kozlowska, M., Yu, W. and Baas, P. W. (2010). Kinesin-12, a mitotic microtubule-associated motor protein, impacts axonal growth, navigation, and branching. *J. Neurosci.* **30**, 14896-14906. doi:10.1523/JNEUROSCI.3739-10.2010
Lowery, L. A. and Van Vactor, D. (2009). The trip of the tip: understanding the growth cone machinery. *Nat. Rev. Mol. Cell Biol.* **10**, 332-343. doi:10.1038/nrm2679
Mack, T. G. A., Koester, M. P. and Pollerberg, G. E. (2000). The microtubule-associated protein MAP1B is involved in local stabilization of turning growth cones. *Mol. Cell Neurosci.* **15**, 51-65. doi:10.1006/mcne.1999.0802
Marco, E. J., Aitken, A. B., Nair, V. P., da Gente, G., Gerdes, M. R., Bologlu, L., Thomas, S. and Sherr, E. H. (2018). Burden of de novo mutations and inherited rare single nucleotide variants in children with sensory processing dysfunction. *BMC Med. Genomics* **11**, 50. doi:10.1186/s12920-018-0362-x
Matov, A., Applegate, K., Kumar, P., Thoma, C., Krek, W., Danuser, G. and Wittmann, T. (2010). Analysis of microtubule dynamic instability using a plus-end growth marker. *Nat. Methods* **7**, 761-768. doi:10.1038/nmeth.1493
McNeely, K. C., Cupp, T. D., Little, J. N., Janisch, K. M., Shrestha, A. and Dwyer, N. D. (2017). Mutation of Kinesin-6 Kif20b causes defects in cortical neuron polarization and morphogenesis. *Neural Dev.* **12**, 5. doi:10.1186/s13064-017-0082-5
Merriam, E. B., Millette, M., Lumbard, D. C., Saengsawang, W., Fothergill, T., Hu, X., Ferhat, L. and Dent, E. W. (2013). Synaptic regulation of microtubule dynamics in dendritic spines by calcium, F-actin, and drebrin. *J. Neurosci.* **33**, 16471-16482. doi:10.1523/JNEUROSCI.0661-13.2013
Miller, K. E. and Sheetz, M. P. (2006). Direct evidence for coherent low velocity axonal transport of mitochondria. *J. Cell Biol.* **173**, 373-381. doi:10.1083/jcb.200510097
Mogessie, B. and Schuh, M. (2017). Actin protects mammalian eggs against chromosome segregation errors. *Science* **357**, eaal1647. doi:10.1126/science.aal1647
Moseley, J. B., Maiti, S. and Goode, B. L. (2006). Formin proteins: purification and measurement of effects on actin assembly. *Methods Enzymol.* **406**, 215-234. doi:10.1016/S0076-6879(06)06016-2
Pardee, J. D. and Spudich, J. A. (1982). Purification of muscle actin. *Meth. Enzymol.* **85**, 164-181. doi:10.1016/0076-6879(82)85020-9
Peleg, S., Sananbenesi, F., Zovoilis, A., Burkhardt, S., Bahari-Javan, S., Agis-Balboa, R. C., Cota, P., Wittnam, J. L., Gogol-Doering, A., Opitz, L. et al. (2010). Altered histone acetylation is associated with age-dependent memory impairment in mice. *Science* **328**, 753-756. doi:10.1126/science.1186088
Pollard, T. D. (1984). Polymerization of ADP-actin. *J. Cell Biol.* **99**, 769-777. doi:10.1083/jcb.99.3.769
Portran, D., Zoccoler, M., Gaillard, J., Stoppin-Mellet, V., Neumann, E., Arnal, I., Martiel, J. L. and Vantard, M. (2013). MAP65/Ase1 promote microtubule flexibility. *Mol. Biol. Cell* **24**, 1964-1973. doi:10.1091/mbc.e13-03-0141
Preciado López, M., Huber, F., Grigoriev, I., Steinmetz, M. O., Akhmanova, A., Koenderink, G. H. and Dogterom, M. (2014). Actin-microtubule coordination at growing microtubule ends. *Nat. Commun.* **5**, 4778. doi:10.1038/ncomms5778
Prezel, E., Stoppin-Mellet, V., Elie, A., Zala, N., Denarier, E., Serre, L. and Arnal, I. (2017). TIRF assays for real-time observation of microtubules and actin coassembly: deciphering tau effects on microtubule/actin interplay. *Methods Cell Biol.* **141**, 199-214. doi:10.1016/bs.mcb.2017.06.012
Qu, X., Yuan, F. N., Corona, C., Pasini, S., Pero, M. E., Gundersen, G. G., Shelanski, M. L. and Bartolini, F. (2017). Stabilization of dynamic microtubules by mDia1 drives Tau-dependent $A\beta_{1\text{-}42}$ synaptotoxicity. *J. Cell Biol.* **216**, 3161-3178. doi:10.1083/jcb.201701045
Rosales-Nieves, A. E., Johndrow, J. E., Keller, L. C., Magie, C. R., Pinto-Santini, D. M. and Parkhurst, S. M. (2006). Coordination of microtubule and microfilament dynamics by *Drosophila* Rho1, Spire and Cappuccino. *Nat. Cell Biol.* **8**, 367-376. doi:10.1038/ncb1385
Roth-Johnson, E. A., Vizcarra, C. L., Bois, J. S. and Quinlan, M. E. (2014). Interaction between microtubules and the *Drosophila* formin Cappuccino and its effect on actin assembly. *J. Biol. Chem.* **289**, 4395-4404. doi:10.1074/jbc.M113.499921
Sabry, J. H., O'Connor, T. P., Evans, L., Toroian-Raymond, A., Kirschner, M. and Bentley, D. (1991). Microtubule behavior during guidance of pioneer neuron growth cones in situ. *J. Cell Biol.* **115**, 381-395. doi:10.1083/jcb.115.2.381
Sahasrabudhe, A., Ghate, K., Mutalik, S., Jacob, A. and Ghose, A. (2016). Formin 2 regulates the stabilization of filopodial tip adhesions in growth cones and affects neuronal outgrowth and pathfinding *in vivo*. *Development* **143**, 449-460. doi:10.1242/dev.130104
Schaefer, A. W., Kabir, N. and Forscher, P. (2002). Filopodia and actin arcs guide the assembly and transport of two populations of microtubules with unique dynamic parameters in neuronal growth cones. *J. Cell Biol.* **158**, 139-152. doi:10.1083/jcb.200203038
Schaefer, A. W., Schoonderwoert, V. T. G., Ji, L., Mederios, N., Danuser, G. and Forscher, P. (2008). Coordination of actin filament and microtubule dynamics during neurite outgrowth. *Dev. Cell* **15**, 146-162. doi:10.1016/j.devcel.2008.05.003
Slater, P. G., Cammarata, G. M., Samuelson, A. G., Magee, A., Hu, Y. and Lowery, L. A. (2019). XMAP215 promotes microtubule-F-actin interactions to regulate growth cone microtubules during axon guidance in Xenopus laevis. *J. Cell Sci.* **132**, jcs224311. doi:10.1242/jcs.224311
Stout, A., D'Amico, S., Enzenbacher, T., Ebbert, P. and Lowery, L. A. (2014). Using plusTipTracker software to measure microtubule dynamics in Xenopus laevis growth cones. *J. Vis. Exp.* **91**, e52138. doi:10.3791/52138
Szikora, S., Földi, I., Tóth, K., Migh, E., Vig, A., Bugyi, B., Maléth, J., Hegyi, P., Kaltenecker, P., Sanchez-Soriano, N. et al. (2017). The formin DAAM is required for coordination of the actin and microtubule cytoskeleton in axonal growth cones. *J. Cell Sci.* **130**, 2506-2519. doi:10.1242/jcs.203455
Tang, N. H. and Chisholm, A. D. (2016). Regulation of microtubule dynamics in axon regeneration: insights from *C. elegans*. *F1000Res* **5**, 764. doi:10.12688/f1000research.8197.1
Thery, M. and Piel, M. (2009). Adhesive micropatterns for cells: a microcontact printing protocol. *Cold Spring Harb. Protoc.* **2009**, pdb.prot5255. doi:10.1101/pdb.prot5255
Turney, S. G. and Bridgman, P. C. (2005). Laminin stimulates and guides axonal outgrowth via growth cone myosin II activity. *Nat. Neurosci.* **8**, 717-719. doi:10.1038/nn1466
Turney, S. G., Chandrasekar, I., Ahmed, M., Rioux, R. M., Whitesides, G. M. and Bridgman, P. C. (2020). Variation and selection in axon navigation through microtubule-dependent stepwise growth cone advance. *bioRxiv*. doi:10.1101/2020.01.29.925602
Vitriol, E. A. and Zheng, J. Q. (2012). Growth cone travel in space and time: the cellular ensemble of cytoskeleton, adhesion, and membrane. *Neuron* **73**, 1068-1081. doi:10.1016/j.neuron.2012.03.005
Vizcarra, C. L., Bor, B. and Quinlan, M. E. (2014). The role of formin tails in actin nucleation, processive elongation, and filament bundling. *J. Biol. Chem.* **289**, 30602-30613. doi:10.1074/jbc.M114.588368

Williamson, T., Gordon-Weeks, P. R., Schachner, M. and Taylor, J. (1996). Microtubule reorganization is obligatory for growth coneturning. *Proc. Natl. Acad. Sci. USA* **93**, 15221-15226. doi:10.1073/pnas.93.26.15221

Zheng, J. Q., Wan, J. J. and Poo, M. M. (1996). Essential role of filopodia in chemotropic turning of nerve growth cone induced by a glutamate gradient. *J. Neurosci.* **16**, 1140-1149. doi:10.1523/JNEUROSCI.16-03-01140.1996

Zhou, F.-Q., Waterman-Storer, C. M. and Cohan, C. S. (2002). Focal loss of actin bundles causes microtubule redistribution and growth cone turning. *J. Cell Biol.* **157**, 839-849. doi:10.1083/jcb.200112014

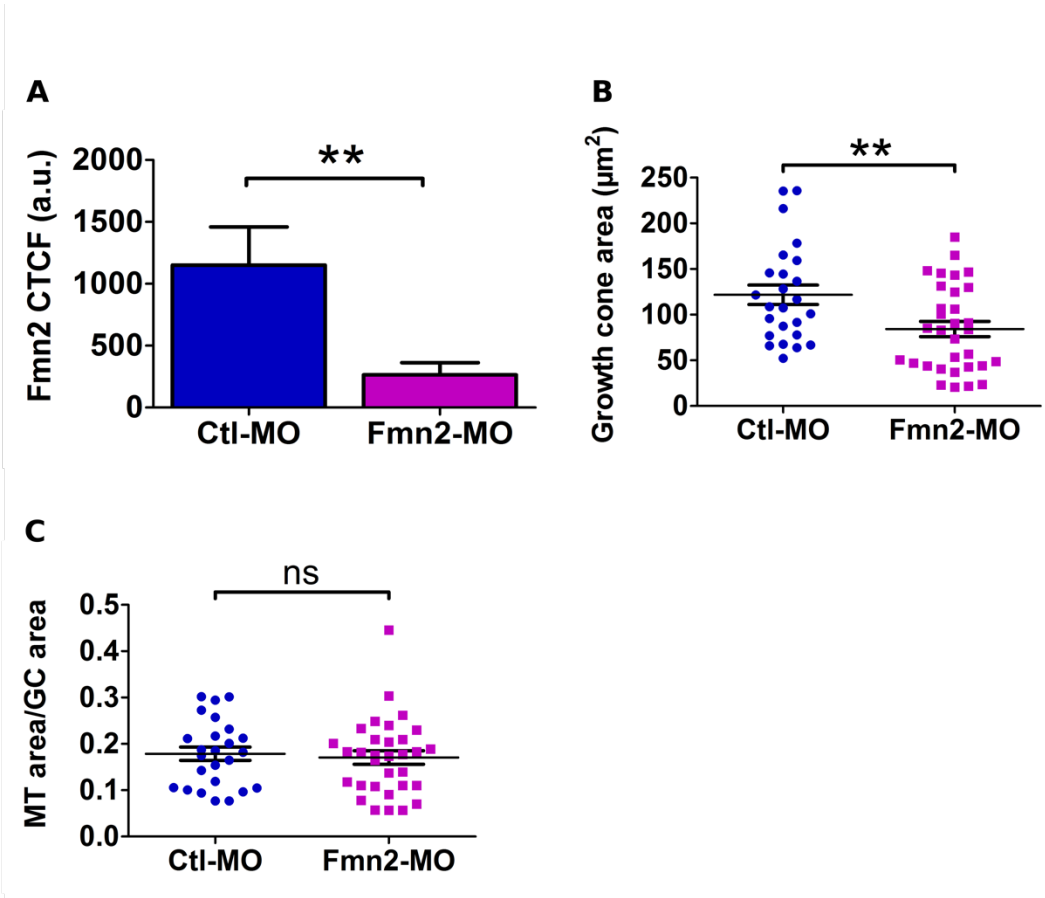

Figure S1. Fmn2 knockdown affects growth cone area.

(A) Quantification of endogenous levels of Fmn2 in Ctl-MO (n=13) and Fmn2-MO (n=10) transfected growth cones of chick spinal neurons; p =0.0026. Corrected total cell fluorescence (CTCF) = Integrated density – (Area of the growth cone x mean background intensity). a.u., arbitray units. (B) Quantification of growth cone area; p =0.0094 and (C) area occupied by MT in the growth cone normalized to growth cone area. The area occupied by microtubules is identified using anti-alpha tubulin antibody and calculated by intensity thresholding within the area outlined as the growth cone; p= 0.5901. (Ctl-MO, n=25; Fmn2-MO, n=32 for both B & C). **P<0.01, ns P>0.05; Mann-Whitney test.

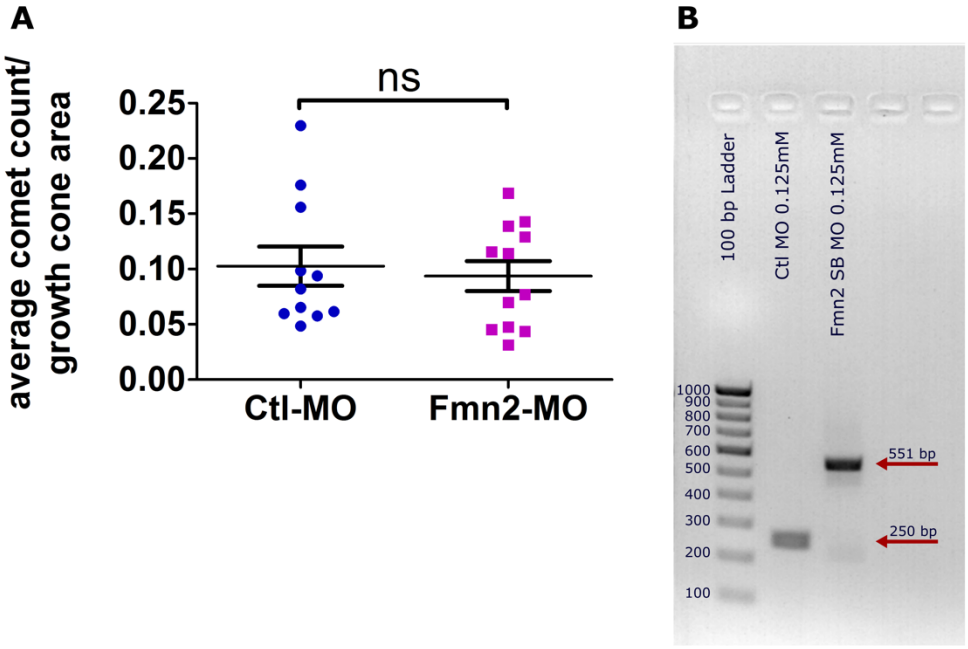

Figure S2. EB3 comets in Ctl-MO and Fmn2-MO growth cones and efficacy of the Zf_Fmn2-MO.

(A) Quantification of average comet count normalized to growth cone area for Ctl-MO (n= 11) and Fmn2-MO (n=12); *p*= 0.6891. ns P>0.05; Mann-Whitney test. (B) RT-PCR with specific primers in exon 5 and 6 of zebrafish Fmn2 shows that the Zf_Fmn2-MO efficiently blocks removal of the intron between exons 5 and 6 leading to a larger amplicon (Lane 3, 551 bp) as compared to control (Lane 2, 250 bp).

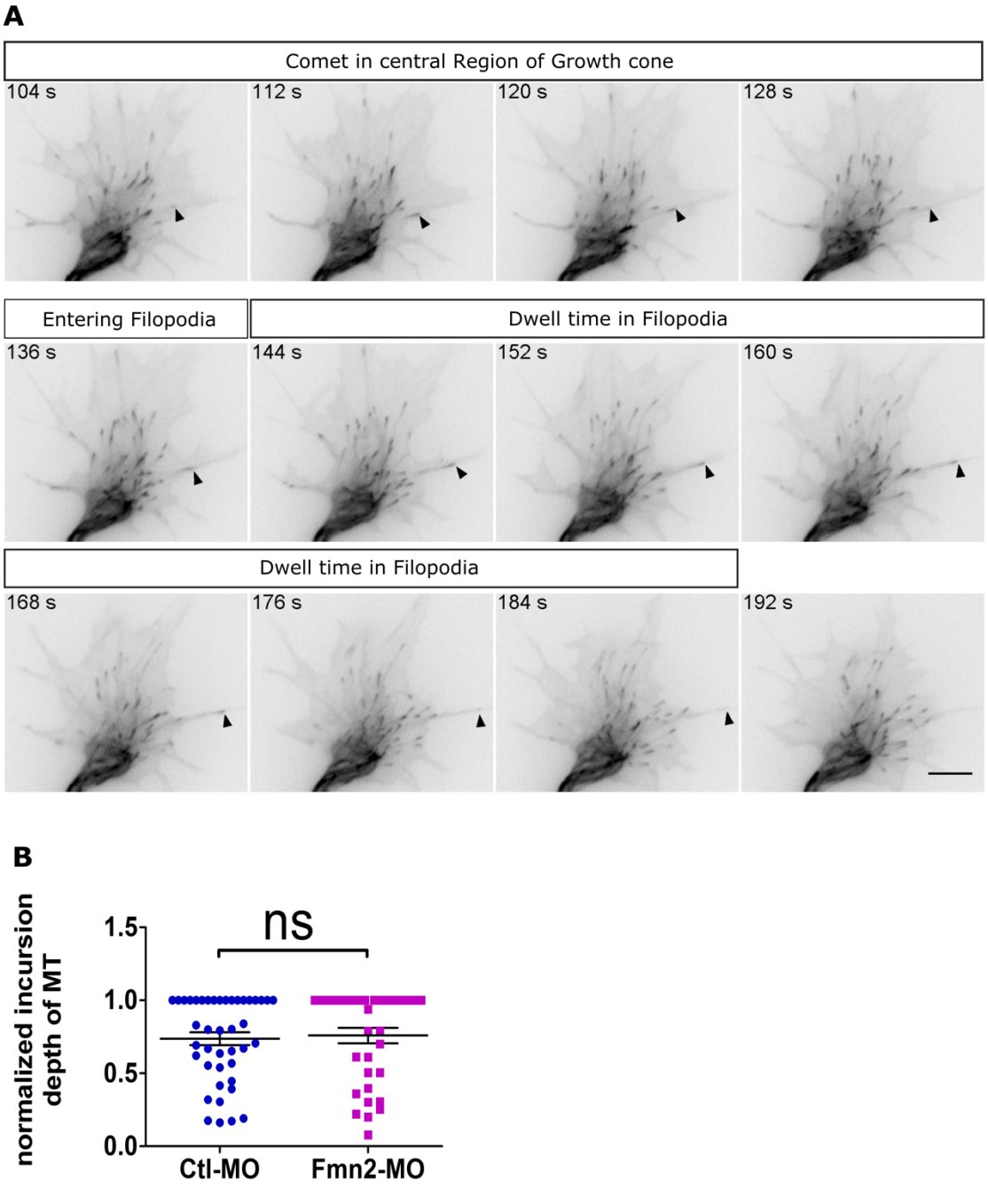

Figure S3. EB3 comets in filopodia.

(A) Representative snapshots of a timelapse series showing EB3 dynamics in a growth cone. The arrowhead marks a EB3 comet entering the filopodia from the central region of the growth cone and its dwell time in the filopodia before it disappears. (B) Quantification of the distance covered by an individual EB3 comet inside filopodia normalized to total filopodial length in Ctl-MO (n= 42) and Fmn2-MO (n= 35) growth cones; *p*= 0.6063. ns P>0.05; Mann-Whitney test.

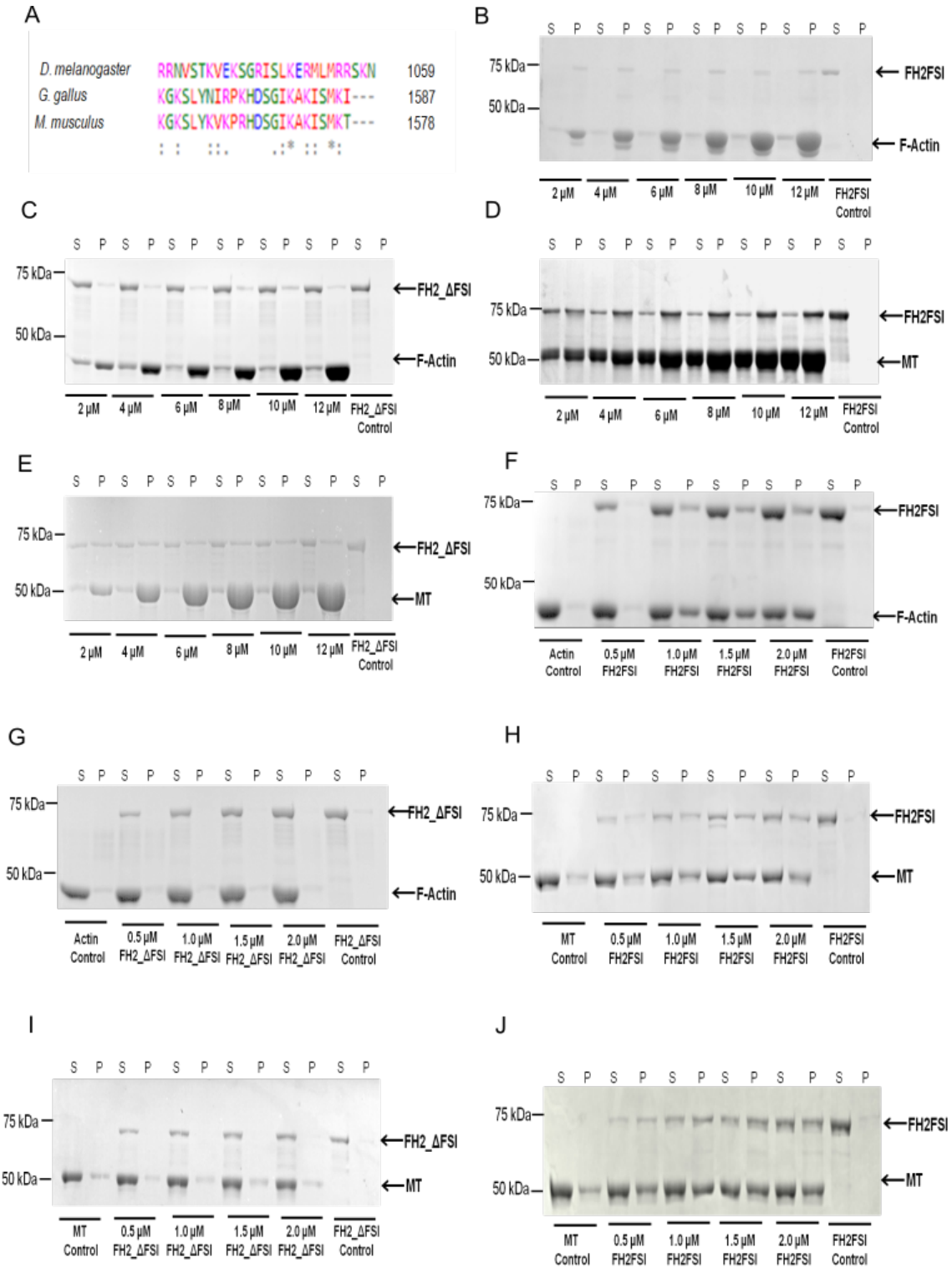

Figure S4. Interaction of Fmn2 with F-actin and Microtubules.

(A) Alignment of FSI domain protein sequences (UniProt Protein Database) for *D. melanogaster* (Q24120), *G. gallus* (A0A1B2VWD2) and *M. musculus* (Q9JL04) using Clustal Omega (1). The colour coding (Magenta: basic amino acids, Green: uncharged polar amino acids, Red: non polar

hydrophobic amino acids, Blue: Acidic amino acids) and the symbols (*conserved residues, **:** strongly similar residues, · weakly similar residue) are used according to the Clustal Omega. (B) High-Speed (320,000 x g) co-sedimentation assay of increasing concentration of F-actin with FH2FSI shows direct interaction between FH2FSI and F-actin. (C) High speed (320,000 x g) co-sedimentation assay of increasing concentration of F-actin with FH2_ΔFSI showing reduced association. (D) High speed (100,000 x g) co-sedimentation assay of MT with FH2FSI shows direct interaction of MT with FH2FSI. (E) High speed (100,000 x g) co-sedimentation assay of FH2_ΔFSI with increasing concentration of MT indicates reduced association. (F) Low speed (10,000 x g) co-sedimentation assay with F-actin indicates bundling of actin filaments in the pellet fraction by FH2FSI. (G) Low speed (10,000 x g) co-sedimentation assay of FH2_ΔFSI with F-actin shows compromised F-actin bundling activity. (H) Bundling of MTs in the pellet fraction in presence of FH2FSI in low speed (5,000 x g) co-sedimentation assay. (I) Reduced MT bundles in the pellet in the presence of FH2_ΔFSI in a low speed (5,000xg) co-sedimentation assay. (J) FH2FSI stabilizes MTs against cold induced depolymerization. Representative SDS-PAGE showing self-assembled MTs are resistance to cold induced depolymerisation when incubated with FH2FSI. After centrifugation at (100,000xg), MTs can be visualized only in the supernatant in the control. With the increasing concentration of FH2FSI, MTs can be visualized in the pellet. Note: In each gel image “S” represents the supernatant fraction and “P” represents the pellet fraction.

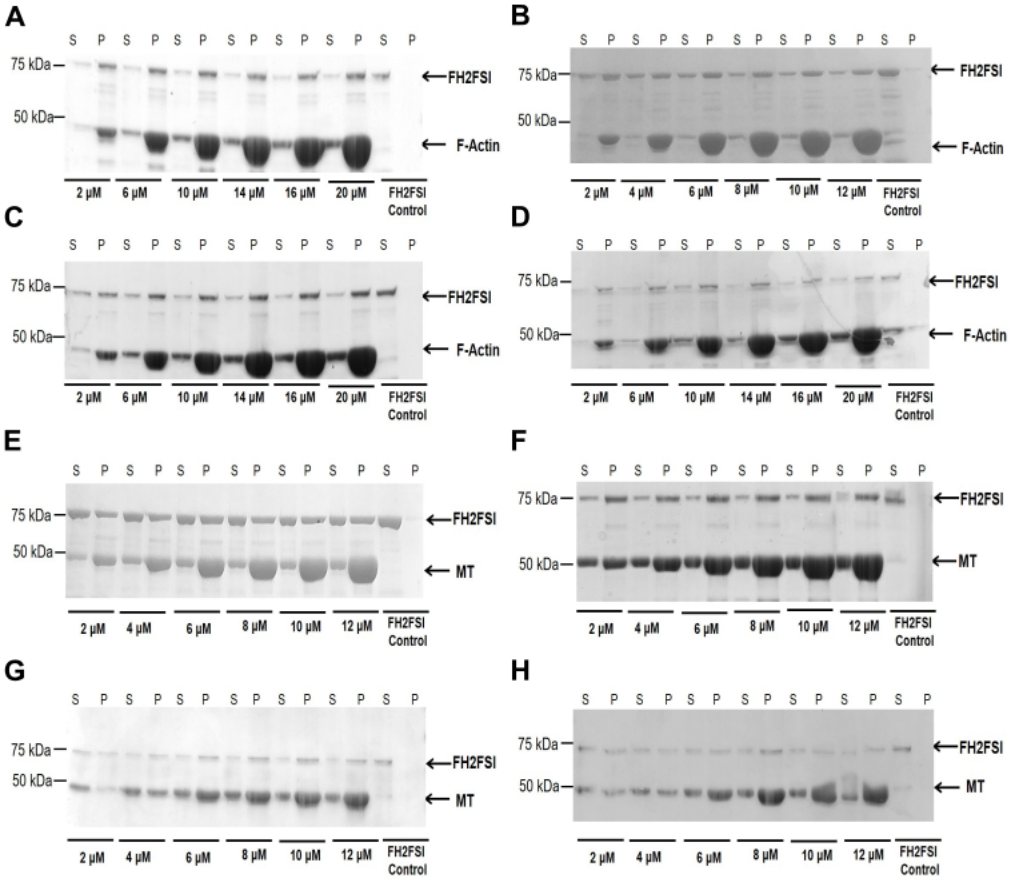

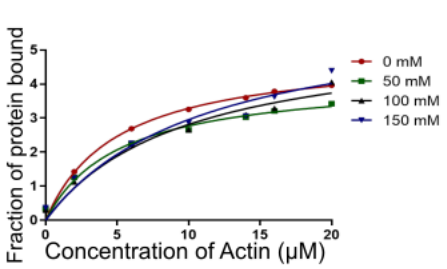

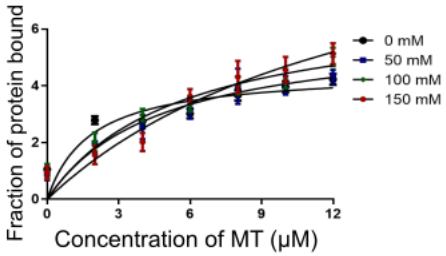

K

	Salt Concentration			
	0 mM	50 mM	100 mM	150 mM
F-Actin Kd (µM)	5.0 ± 0.2	5.2 ± 0.2	9.7 ± 0.8	11.2 ± 0.5
Microtubule Kd (µM)	1.8 ± 0.4	4.8 ± 0.6	5.6 ± 0.5	14.2 ± 0.3

Figure S5. Interactions of Fmn2 with F-actin and MTs at varying salt concentrations.

Co-sedimentation assay shows the binding of FH2FSI with increasing concentration of F-actin at (A) 0 mM KCl, (B) 50 mM KCl (C) 100 mM KCl and (D) 150 mM KCl. FH2FSI also co-sediments with MTs at (E) 0 mM KCl, (F) 50 mM KCl, (G) 100 mM KCl and (H) 150 mM KCl. (I) Binding kinetics of FH2FSI to F-actin in the presence of varying salt concentrations. Increasing concentrations of F-actin was incubated with 2 µM of FH2FSI at pH 7.5. The percentage of bound

proteins from each concentration of salt was plotted against F-actin concentrations and fitted with a hyperbolic function. The Kd_{app} for FH2FSI for different concentration of salt is 5.0 ± 0.2 μM (0 mM of KCl), 5.2 ± 0.2 μM (50 mM KCl), 9.8 ± 0.8 μM (100 mM KCl), and 11.2 ± 0.5 μM (150 mM KCl); (mean ± SD from three independent experiments). (J) Binding of FH2FSI to MTs in the presence of varying salt concentrations. Increasing concentrations of MTs was incubated with 2 μM of protein at pH 7.5. The percentage of bound proteins from each concentration of salt was plotted against MT concentrations and fitted with a hyperbolic function. The Kd_{app} for FH2FSI for different concentration of salt is 1.8 ± 0.4 μM (0 mM of KCl), 4.8 ± 0.6 μM (50 mM KCl), 5.6 ± 0.5 μM (100 mM KCl), and 14.2 ± 0.3 μM (150 mM KCl); (mean ± SD from three independent experiments). (K) Tabular representation of the Kd_{app} for FHSFSI binding F-actin or MT at various salt concentration. Note: In each gel image “S” represent the supernatant fraction and “P” represent the pellet fraction.

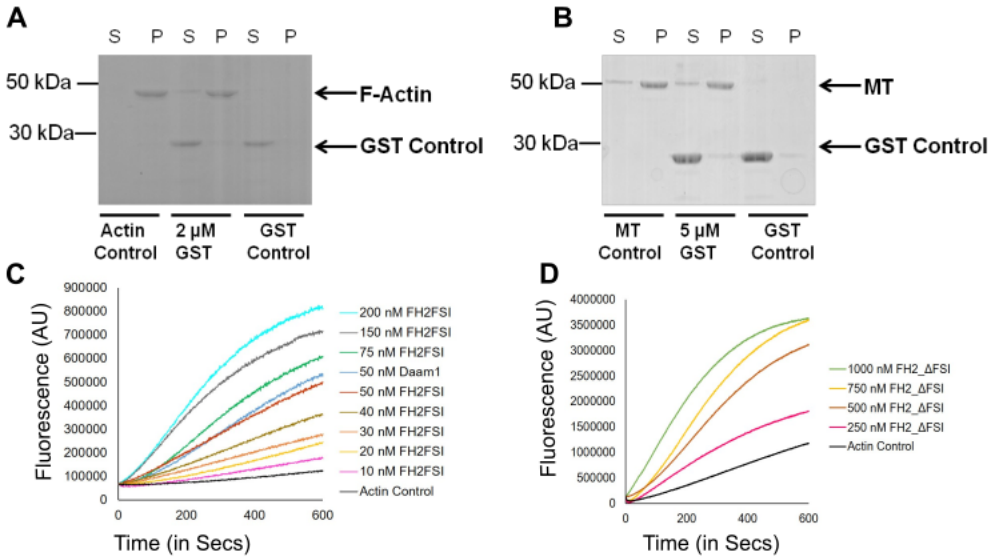

Figure S6. The functional activity of recombinant FH2FSI and FH2_ΔFSI fragments.

Recombinant GST protein does not bind to (A) preformed F-actin or (B) MTs in high-speed co-sedimentation assay indicating specificity for GST fusion protein used in this study. (C) Time course of pyrene-actin nucleation assay with the indicated concentrations of the FH2FSI domain of Fmn2 and Daam1 (positive control). 2 µM actin (10% pyrene-labelled) and indicated (nM) concentrations of FH2FSI protein was used. (D) Time course of pyrene-actin nucleation assay with the indicated concentrations of the FH2_ΔFSI domain of Fmn2. 2 µM actin (10% pyrene-labelled) and indicated concentrations of FH2_ΔFSI was used.

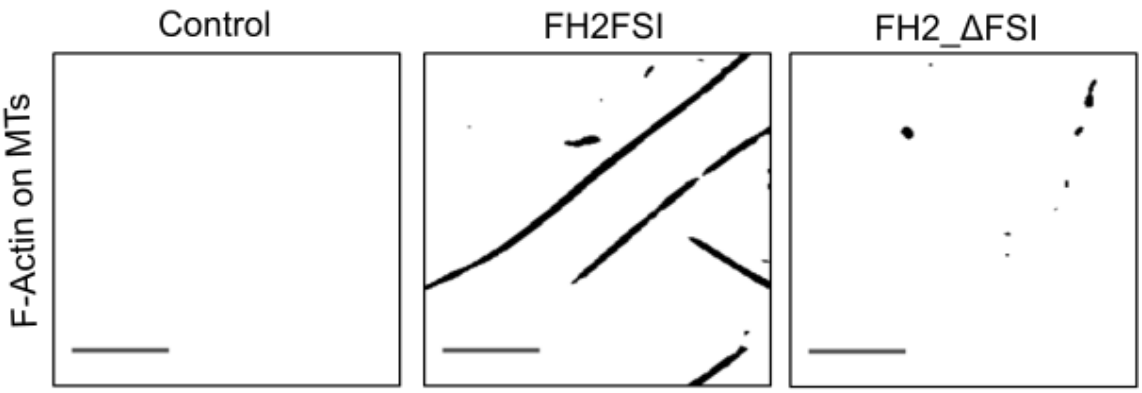

Figure S7. Fmn2 cross-bridges polymerizing Microtubules and F-actin filaments

The masked images represent the actin area that co-localizes with microtubule in the last frame of the movies in Control, FH2FSI and FH2_ΔFSI respectively. Scale bar 10 μm.

Table S1. Plasmid constructs used in this study indicating source, vector backbone, cloning strategy and primers used for cloning.

Plasmid name	Plasmid backbone	Insert name	Source	Gene bank acc no	Primers used for cloning	Region cloned and cloning strategy
pCAG-GFP	pCAG	-	Addgene (111500)	-	-	-
pCAG-mCherry	pCAG	mCherry	This study	-	Fwd 5'ATATATACCGGTCGCCACCATGGTGAGCAAGGGCGAGGAGG3' Rev 5'ATATATGCGGCCGCTTTACTTGTACAGCTCGTCCATGCCGCC3'	cloned by ligation between AgeI and NotI sites
pCAG-EB3-GFP & pCAG-EB3-mCherry	pCAG-GFP & pCAG-mCherry	EB3; Gift from Dr. Anna Akhmanova, Utrecht University	This study	NM_012326	Fwd - 5'GCAAAGAATTCTGCAGTCGACGGTACCCGCCACCATGGCCGTCAATGTGTACTCC3' Rev- 5'CCATGGTGGCGACCGGTGGATCCCGGGTTAAGTACTCGTCCTGGTCTTCTTG3'	complete cds, cloned using homologous recombination between KpnI and XmaI
pCS2-GFP-Tubulin	pCS2-GFP	Alpha tubulin	Gift from Dr. Ulrike Engel, University of Heidelberg	NM_00608	-	-
pCAG-mFmn2-FL-GFP	pCAG-GFP	mFmn2; Gift from Dr. Philip Leder, Harvard	This study	NM_019445	Fwd- 5'AGTCGACGGTACCCGCCACCATGGGGAACCAGGATGGGAAG 3' Rev-	complete cds, cloned between KpnI and XmaI

		Medical School			5'GGTGGCGACCGGTGGATCCCGGGtCGTTTTCATGCTTATCTTCGCTTTAATC 3'	
pCAG-mFmn2-ΔFSI-GFP	pCAG-GFP	pCAG-mFmn2-FL-GFP	This study	NM_019445	Fwd-5'GCAAAGAATTCTGCAGTCGACGGTACCCGCCACCATGGGGAACCAGGATGG 3' Rev 5'CCATGGTGGCGACCGGTGGATCCCGGGCCTTCTGCCTACACACCTCC3'	1-4662, cloned by Homologous recombination between KpnI and XmaI
pGEX-6P1-cFH2FSI	pGEX-6P1	FH2FSI	This study	KU711529.1	Fwd-5'GCGGGATCCGGGAGCAGGAAACATGTGATAG3' Rev-5'GGAAGGAAAAAAGCGGCCGCTTAGATTTTCATACTTATCTTGGCTTTAATTC3'	3436-4761 (1148-1587aa), cloned by double digestion and ligation using BamHI and NotI
pGEX-6P1-cFH2_ΔFSI	pGEX-6P1	FH2_ΔFSI	This study	KU711529.1	Fwd-5'GCGGGATCCGGGAGCAGGAAACATGTGATAG3' Rev-5'GGAAGGAAAAAAGCGGCCGCTTATTTCTGTCTGCAGACTTCCTCTG3'	3436-4689 (1148-1563aa), cloned by double digestion and ligation using BamHI and NotI
pEXP-*3.1ngn1*:TagRFP-CAAX	pEXP (Gateway destination vector)	-	Gift from Dr. Mary Halloran, UW-Madison	-	-	-
pEXP-*3.1ngn1*:EB3-GFP	pEXP (Gateway destination vector)	-	Gift from Dr. Mary Halloran, UW-Madison	-	-	-

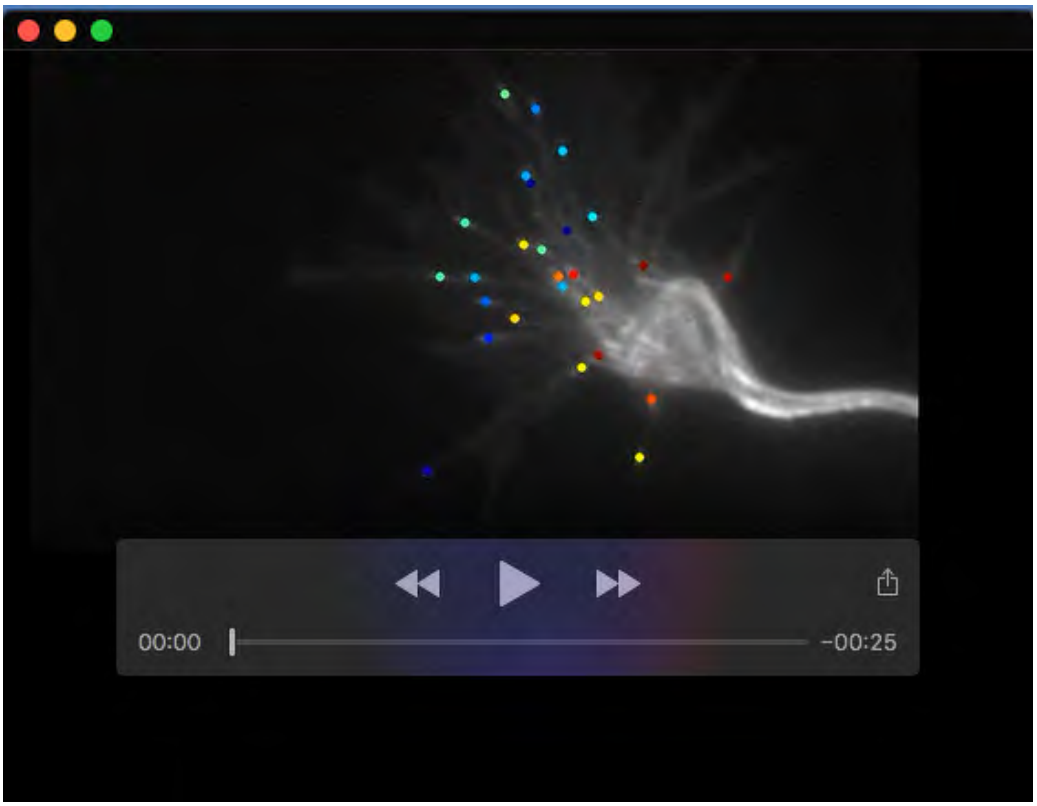

Movie 1. Ctrl-MO transfected growth cone displaying EB3-GFP comets. The EB3 comets are color-coded in correspondence with increasing growth speed (blue to red) using the plustiptracker software.

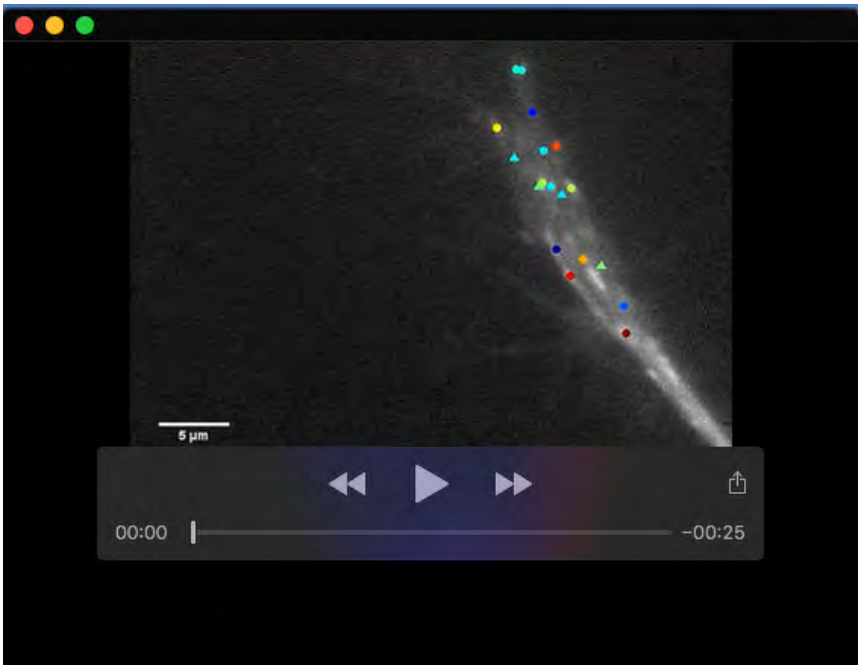

Movie 2. Fmn2-MO transfected growth cone displaying EB3-GFP comets. The EB3 comets are color-coded in correspondence with increasing growth speed (blue to red) using the plustiptracker software.

Journal of Cell Science • Supplementary information

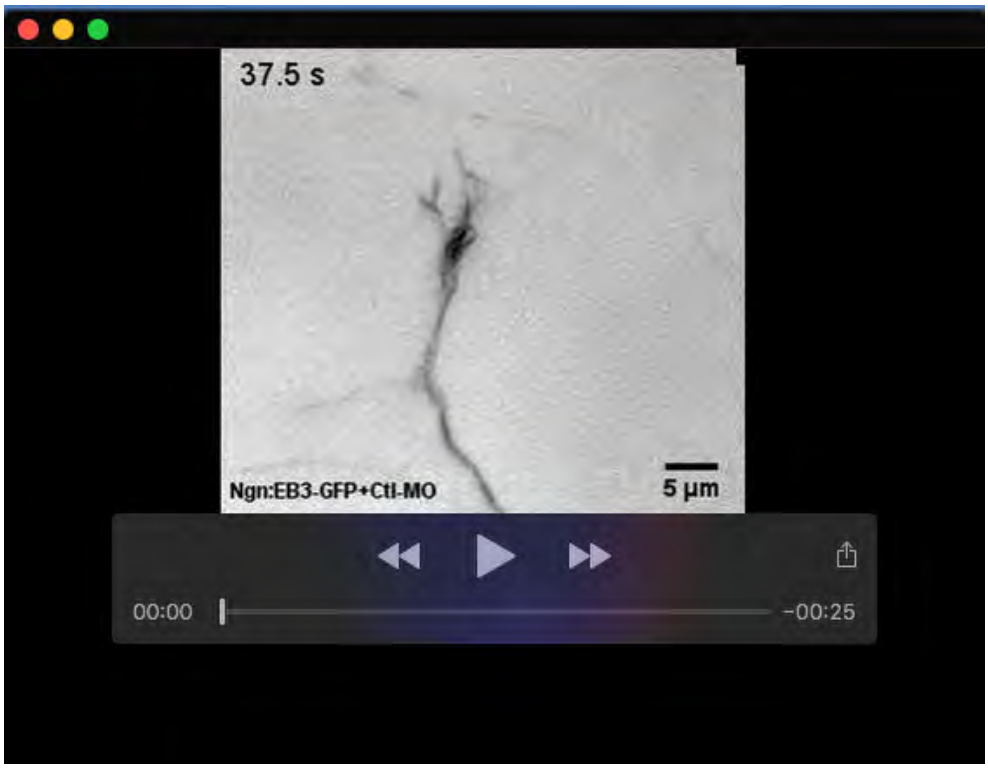

Movie 3. RB neuron growth cone of a Ctl-MO injected zebrafish displaying EB3 comets *in-vivo*.
Timelapse video of EB3-GFP in the growth cone of the peripheral axon of an RB neuron of a 22 hpf zebrafish embryo injected with Ctl-MO.

Movie 4. RB neuron growth cone of a Zf_Fmn2-MO injected zebrafish displaying EB3 comets *in-vivo*.
Timelapse video of EB3-GFP in the growth cone of the peripheral axon of an RB neuron of a 22 hpf zebrafish embryo injected with Zf-Fmn2-MO.

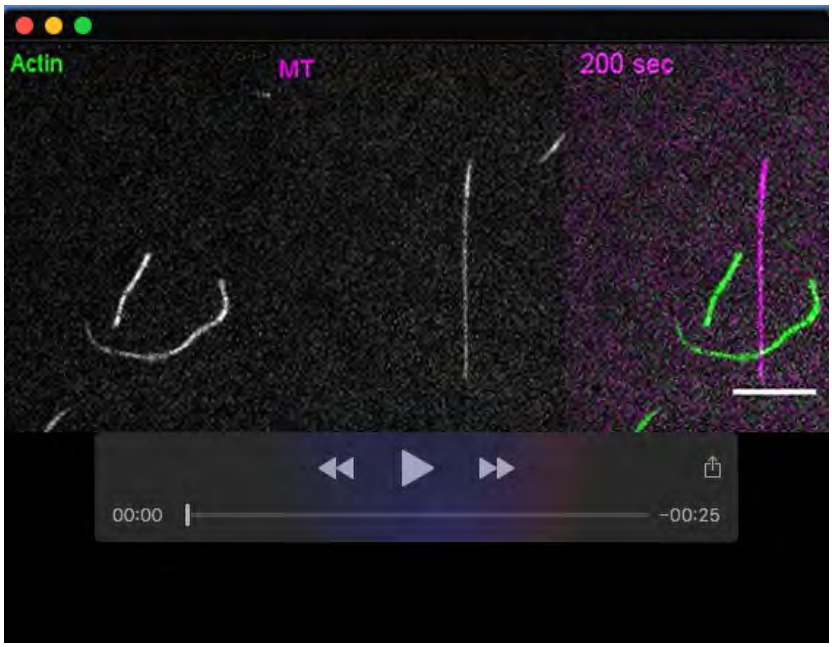

Movie 5. Co-polymerization of actin and tubulin in the absence of protein.
Dual colour TIRFM timelapse video of actin (green) and tubulin (magenta), polymerizing together in absence of protein. The time (in secs) represents the elapsed time start from the acquisition. The scale bar is 10 μm.

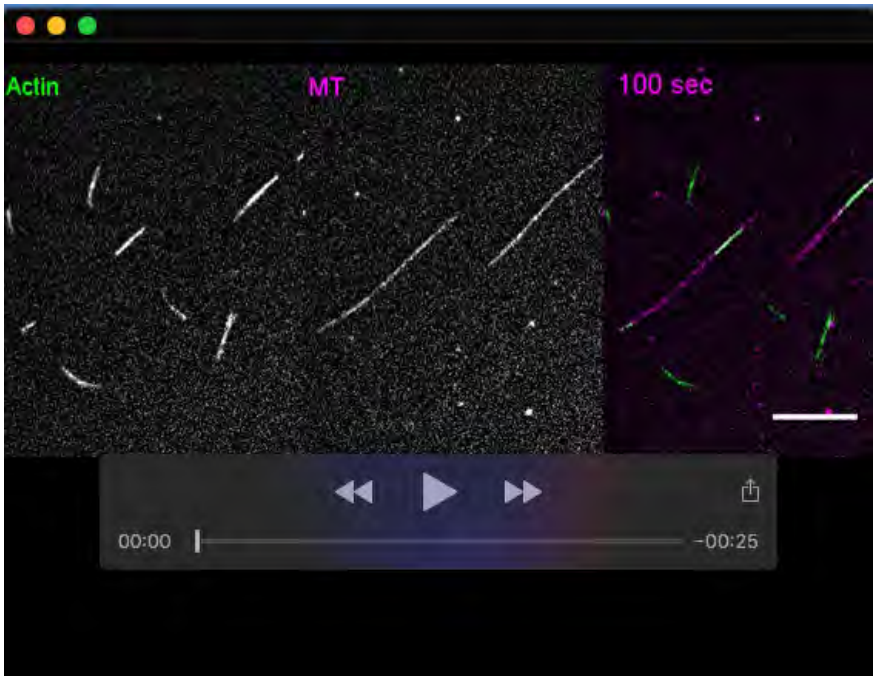

Movie 6. Co-polymerization actin and tubulin in the presence of FH2FSI.
Dual colour TIRFM timelapse video of FH2FSI induced co-assembly of actin (green) and tubulin (magenta). The time (in secs) represents the elapsed time start from the acquisition. The scale bar is 10 μm.

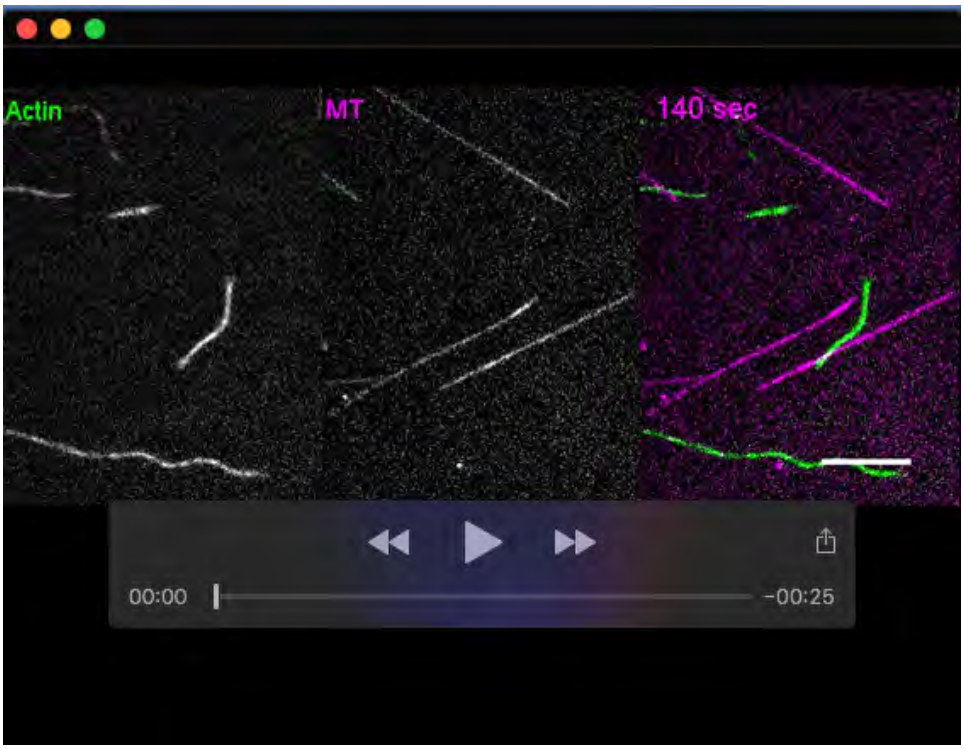

Movie 7. Co-polymerization of actin and tubulin in the presence of FH2_ΔFSI. Dual colour TIRFM timelapse video of actin (green) and tubulin (magenta), polymerizing together in presence of FH2_ΔFSI. The time (in secs) represents the elapsed time start from the acquisition. The scale bar is 10 µm.